Review Article

Nano Research
2023, 16(7): 8614–8637

ISSN 1998-0124 CN 11-5974/O4
https://doi.org/10.1007/s12274-023-5576-3

Recent progress of two-dimensional metal-organic-frameworks: From synthesis to electrocatalytic oxygen evolution

Huakai Xu, Xiaofei Wei, Hui Zeng, Chuanhai Jiang, Zhifei Wang, Yuguo Ouyang, Chunyu Lu, Yuan Jing, Shiwei Yao, and Fangna Dai (✉)

School of Materials Science and Engineering, China University of Petroleum (East China), Qingdao 266580, China

Received: 29 December 2022 / **Revised:** 9 February 2023 / **Accepted:** 13 February 2023

ABSTRACT

High-performance electrocatalysts for oxygen evolution reaction (OER) are crucial for water splitting and metal-air batteries. Two-dimensional (2D) metal-organic framework (MOF) has become a new class of efficient OER electrocatalysts due to the rich coordination unsaturated metal nodes, large specific surface area, and adjustable structures. In addition, because inheriting the original microstructure of MOFs and having stronger chemical and mechanical stability, metal/alloy/oxide, metal sulfide/selenide/phosphide, and other compounds derived from 2D MOFs have also shown their unique OER catalytic ability. Here, we briefly introduced the existing reaction mechanism and evaluation parameters of catalyst performance of OER, introduced the synthesis methods and corresponding characterization techniques of 2D MOFs and their derivatives, and summarized the latest progress of 2D MOFs and their derivatives as OER catalysts. Finally, we put forward some views and suggestions on the existing problems hindering the development of 2D MOFs as OER for advancing the field.

KEYWORDS

two-dimensional metal-organic framework, derivatives, synthesis, catalysis, oxygen evolution reaction

1 Introduction

Water electrolysis technology (Fig. 1(a)) and rechargeable metal-air batteries (Fig. 1(b)) have been widely used in energy storage and conversion due to their environmentally friendly, efficient, and safe features [1–3]. As the key electrochemical reaction involved in these devices, the electrochemical oxygen evolution reaction (OER) has attracted much attention [4, 5]. OER is an oxidation of H_2O or OH^- to oxygen and is ideally carried out near the thermodynamic limit of 1.23 V [6]. However, OER involves a multi-electron transfer process whether in acidic or alkaline environments, resulting in slow reaction kinetics and high overpotential for OER [7, 8]. According to the widely recognized oxygen evolution pathway (adsorbate evolution mechanism (AEM)), the reaction processes in acidic solution are as follows [9]

$$H_2O \rightarrow {}^*OH + H^+ + e^-$$

$$^*OH \rightarrow {}^*O + H^+ + e^-$$

$$^*O + H_2O \rightarrow {}^*OOH + H^+ + e^-$$

$$^*OOH \rightarrow O_2 + H^+ + e^-$$

while in alkaline solution are as follows

$$OH^- \rightarrow {}^*OH + e^-$$

$$^*OH + OH^- \rightarrow {}^*O + H_2O + e^-$$

$$^*O + OH^- \rightarrow {}^*OOH + e^-$$

$$^*OOH + OH^- \rightarrow O_2 + H_2O + e^-$$

The unfavorable factors of OER seriously limit the further development of these energy conversion and storage devices. Therefore, accelerating dynamics rate by developing effective and stable OER electrocatalysts can significantly improve the energy conversion efficiency.

Metal-organic frameworks (MOFs), a crystalline porous material composed of transition metal and organic ligands, have been extensively researched for gas separation [10, 11], sensing [12, 13], biomedicine [14], and catalysis because of the large surface area, ultra-high porosity, versatile functionalization, and special topological structure. However, the small pore size and low accessibility of active sites of most bulk MOFs decelerate the mass and charge transfer processes, resulting that high interface resistance limits the application of MOFs (especially bulk MOFs) in the catalytic field [15]. Inspired by two-dimensional (2D) materials such as graphene and boron nitride, 2D MOFs not only have the advantages of MOFs material structure, but also overcome the shortcomings of bulk MOF to a certain extent (Fig. 1(c)) [16–19]. Compared with other-dimensional MOF, 2D MOF has the following advantages: (1) The larger accessible surface of 2D MOFs can provide more unsaturated sites for OER. (2) The ultra-thin sheet structure can effectively promote the adsorption of

Address correspondence to fndai@upc.edu.cn

reactants and the transfer of products in OER. (3) 2D MOFs are easy to be prepared into films, thus closely fitting with the electrode, avoiding the limitation that bulk materials are easy to fall off automatically, and improving the service life of the electrode in OER reaction [20, 21]. However, due to the complex synthesis and difficult preparation of 2D MOF, the number of 2D MOFs used for OER reaction is far less than that of non-2D MOFs (Fig. 1(d)). In addition, 2D MOF is also connected by metal nodes and organic ligands, and its conductivity and stability need to be improved. Therefore, it is a feasible way that converting 2D MOFs materials into their derivatives (such as hydroxides [22], carbon-based nanosheet-supported alloys [23], metal oxides [24], metal sulfides [25], metal phosphides [26], metal selenides [27], and metal carbides) to enhance conductivity and stability, thus improving the (OER) catalytic ability of the material. 2D MOFs derivatives generally maintain the same ultra-thin structure as 2D MOFs, which can improve the catalytic efficiency of materials. But unlike MOFs, 2D MOF derivatives have better excellent chemical and mechanical stability due to stronger binding bond, which can ensure structural stability in the OER catalytic process. These advantages of 2D MOF derivatives will be more conducive to efficient catalytic OER. Figure 1(e) shows the proportion of various 2D MOF derivatives for OER. In recent years, a large number of 2D MOFs and their derivatives have been reported as OER catalysts, but rarely organized and summarized. Therefore, a comprehensive overview is needed to summarize the progress, and provide feasible suggestions for the further development for 2D MOFs and their derivatives as OER catalysts.

Here, this work reviews the application progress of 2D MOFs in catalytic OER from the following aspects. Firstly, the mechanisms and basic parameters of OER are introduced to provide a standard for measuring the OER catalytic performance of the materials mentioned below. Then, the design principle and synthesis strategy of 2D MOFs and derivatives are evaluated. And then, some characterization methods are introduced. Finally, the application of 2D MOFs and their derivatives in OER is emphatically introduced. Through the discussions in this review, we hope to provide some perspectives on how to achieve efficient electrocatalytic OER by rationally designing 2D MOFs and their derivatives.

2 Mechanisms and evaluation parameters for OER

2.1 Mechanisms

The reaction mechanism of OER is generally considered to be through two ways: adsorbent evolution mechanism (AEM) (Fig. 2(a)) and lattice oxygen mediated mechanism (LOM) (Fig. 2(b)) [6, 9]. At present, Xi et al. have proposed a new OER route, named coupled oxygen evolution mechanism (COM) (Fig. 2(c)) [28]. AEM is an electron transfer process in which the metal band near

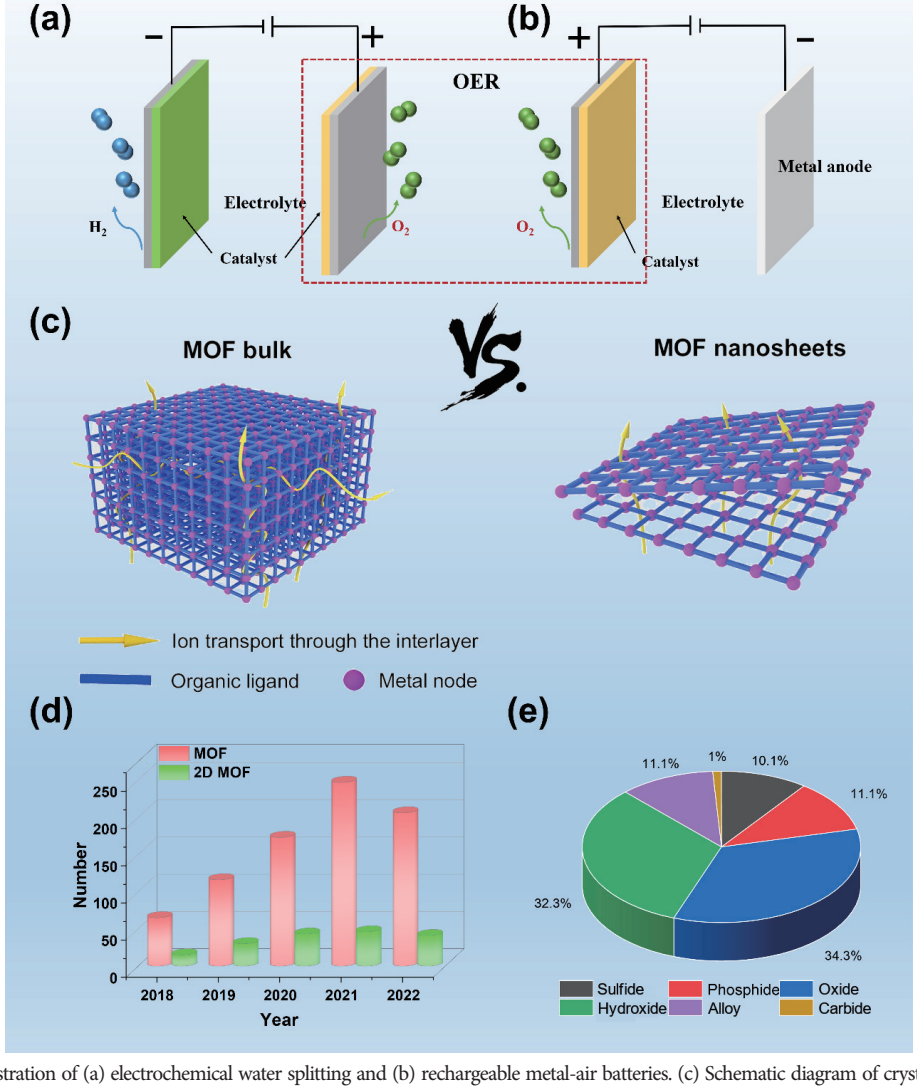

Figure 1 Schematic illustration of (a) electrochemical water splitting and (b) rechargeable metal-air batteries. (c) Schematic diagram of crystal structure of MOF and 2D MOF. Reproduced with permission from Ref. [180], © Elsevier B.V. 2020. (d) Summary of publications of MOF materials used in OER in recent years (2018–2022), searched using the "Web of Science". (e) The proportion of various 2D MOF derivatives for OER.

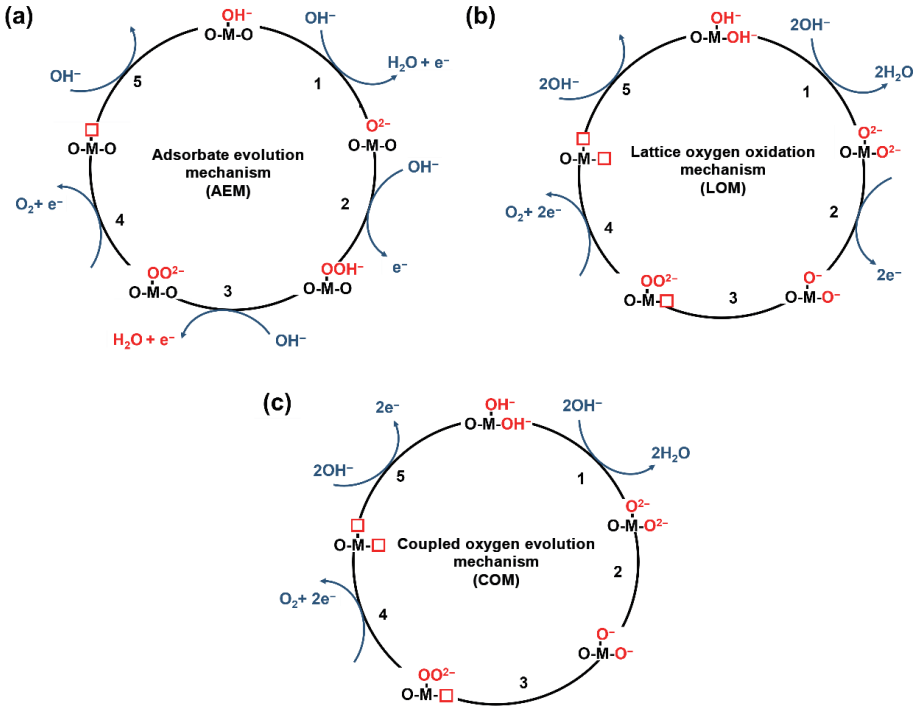

Figure 2 The reaction route of (a) adsorbent evolution mechanism, (b) lattice oxygen mediated mechanism, and (c) coupled oxygen evolution mechanism.

the Fermi level acts as the redox center of OER. The reaction overpotential is affected by the bonding strength of the intermediate on the surface of catalyst [29]. LOM is an electron transfer process in which the oxygen band near the Fermi level acts as the redox center of OER. The reaction overpotential is not only affected by the binding strength of the intermediate on the surface of catalyst, but also related to the oxygen of the catalyst. COM is an electron transfer process involving the redox reaction between oxygen and metals. Its deprotonation takes place on the metal band, and the O–O coupling process takes place on the oxygen state [28].

2.1.1 *Traditional adsorbate evolution mechanism*

AEM is generally considered to involve four proton electron transfer reactions centered on active metal sites, following the paths of OH*, O*, OOH*, and O_2. As shown in Fig. 2(a), in the deprotonation step (from OH* to O*), the break of the O–H bonds is accompanied by an electron and proton transfer. The transfer of electrons from the metal to the outside causes the increase of the valence state of the metal site. During the formation of OOH*, the adsorption of OH^- from the electrolyte leads to the transfer of an electron and a proton. To realize the 8-electron configuration of oxygen, two electrons must be transferred from oxygen to metal, which will reduce the valence state of metal site. The subsequent deprotonation step (from OOH* to OO*) also involves the breaking of O–H bonds. In this process, electrons are transferred from the metal to the outside, thus increasing the valence state of metal site. In the oxygen evolution step, one electron is transferred from the metal to the outside and two electrons are transferred from oxygen to the metal. In general, the valence state of metal site decreases in this step.

2.1.2 *Lattice-oxygen-mediated mechanism*

In the AEM route, the surface of catalyst is considered as a stable platform, and only the valence state of metal site changes during the oxygen oxidation process. However, in the LOM pathway, the catalytic surface is no longer a stable platform, and will change with the oxygen oxidation process. The oxidation, coupling, and release of lattice oxygen on the surface of catalyst are necessary for LOM path cycling. As shown in Fig. 2(b), the traditional LOM process includes deprotonation, O–O coupling, and O_2 release. In the deprotonation step, the break of O–H bond causes a proton to remove from OH* to the outside. At the same time, the adsorbed OH* will be converted to O^{2-}. To achieve O–O coupling, O^{2-} will be converted to O^-. Therefore, an electron is transferred from the O^{2-} to the outside to keep the 8-electron configuration of oxygen. In the oxygen evolution step, two electrons must be removed from the oxygen orbit of $(O–O)^{2-}$ to achieve the electronic structure of O_2. In a word, during the deprotonation step, oxygen transferred two electrons to the outside, and during the O_2 generation step, oxygen transferred two electrons to the outside again, which is summarized as four electron transfer processes during OER, only oxygen acts as metal redox center. *OOH is not formed in a typical LOM route, so the limitation of AEM can be broken.

The concept of LOM was first proposed by Damjanovic and Jovanovic in 1976 [30]. In 2015, Binninger et al. proposed a more formal description and coined the term lattice oxygen evolution reaction [31]. Stevenson et al. confirmed that lattice oxygen participating in the OER process can enhance its intrinsic activity and accelerate the reaction kinetics through in-depth research on the OER process on different perovskite oxides [32, 33]. In 2017, Shao-Horn et al. directly proved that the O_2 generated by some highly active oxides in the OER process can come from lattice oxygen through *in situ* ^{18}O isotope labeling mass spectrometry [34]. At present, the origin of the intrinsic activity of various solid transition metal oxides (TMOs) [35–37] and transition metal (oxy)hydroxides [4, 38–40] is well understood through LOM.

2.1.3 *Light-triggered coupled oxygen evolution mechanism*

COM is proposed by Xi et al. in 2022 [28]. Compare with AEM and LOM, COM possibly contains two types of redox activities: metal redox activities with electron transfer from metal electronic states and oxygen redox activities with electron transfer from non-bonding oxygen states. As shown in Fig. 2(c), COM also involves the processes of deprotonation, O–O coupling, and O_2 release. Different from LOM, in the O–O coupling step (O^{2-} is converted to O^-), to maintain the 8-electron configuration of oxygen,

electrons are transferred from oxygen to metal rather than the outside, and the octahedral configuration of MO_6 is transformed into the planar configuration of MO_4. In addition, to restore the octahedral configuration of MO_6, electrons are transferred from metal to the outside in the OH^- adsorption step.

2.2 Evaluation parameters

2.2.1 Overpotential (η)

Ideally, the OER requires a voltage of 1.23 V to proceed. Due to the inherent kinetic barrier, an additional potential larger than the equilibrium voltage is required to start the reaction of OER in practice. The potential difference between the electrode potential and the electrode equilibrium potential (1.23 V vs. reversible hydrogen electrode (RHE)) is defined as the overpotential [41]. The role of the catalyst is to reduce the overpotential. At a given current density, the smaller the overpotential value, the higher the electrochemical catalytic activity of the catalyst. Since the current density corresponding to 10% conversion efficiency in solar water splitting cells under unit time illumination is about 10 $mA·cm^{-2}$, the performance of the catalyst is usually measured by comparing the overpotential at the current density of 10 $mA·cm^{-2}$ [42].

2.2.2 Tafel slope

Tafel slope is an electrochemical kinetic parameter that correlates the overpotential with the electrochemical reaction rate [43]. And it can be calculated as follows: $\eta = a + b \times \log j$, where η is the overpotential, b represents the Tafel slope, and j denotes the current density. Especially for the Tafel slope of oxygen evolution reaction, if the value is equal to 120 $mV·dec^{-1}$, it indicates that the rate determination step is the first step, that is, the rate control step in the reaction is determined by the single electron transfer step. If the value is 40 or 60 $mV·dec^{-1}$, the rate determination step is the second step. For the existing model, analyzing the third or fourth step will be more complex [41].

2.2.3 Turnover frequency (TOF)

TOF represents the inherent catalytic activity of the catalyst, which is defined as the number of molecules reacting at the catalytic site per unit time, and can be measured according to the equation: $\mathrm{TOF} = \frac{jA}{\alpha Fn}$, where j is the current density, A is the surface area of the working electrode, α is the number of electrons transferred, F represents the Faraday constant, and n is the number of moles (mol) of gas molecules generated on the electrode.

2.2.4 Electrochemical active surface area (ECSA)

To evaluate the true catalytic activity of the materials, the researchers introduced the ECSA to analyze the actual surface area involved in the electrochemical catalytic reaction. Due to the electric double layer capacitance (C_{dl}) is proportional to ECSA of the catalyst, ECSA of the catalyst can be obtained by calculating the value of C_{dl}.

2.2.5 Stability

In addition to excellent activity, stability is also an important indicator for evaluating the quality of catalysts and is a prerequisite for large-scale commercial applications. In general, two methods are frequently used to measure the stability of electrocatalysts. One is comparing the changes in the linear sweep voltammetry (LSV) curve before and after thousands of cyclic voltammetry (CV) cycles. Another is measuring the stable duration of the corresponding potential (current density) of the catalyst through chronoamperometry (chronopotentiometry) [44, 45].

3 Synthetic strategy and characterization of 2D MOF and derivatives

3.1 Synthesis of 2D MOF

2D MOFs have attracted widespread attention due to potential structural advantages. However, the cost of 2D MOFs increases exponentially with the specificity of organic ligands and the complexity of synthesis steps. How to obtain low cost and high yield 2D MOF nanosheets (NSs) by gentle methods remains a great challenge [46, 47]. As shown in Fig. 3(a), various methods for synthesizing ultra-thin 2D MOF have been explored. In general, the effective preparation strategies of 2D MOFs can be divided into two categories: top-down peeling and bottom-up assembly (Fig. 3(b)) [48–52]. For clarity, Table 1 summarizes partial literatures on reported 2D MOF synthesis strategy and Fig. 4 lists the corresponding ligand structures. 2D MOFs prepared by different synthesis methods have different catalytic effects on OER. For example, 2D MOF sheets prepared by top-down peeling method can expose more active sites due to the peeling of the

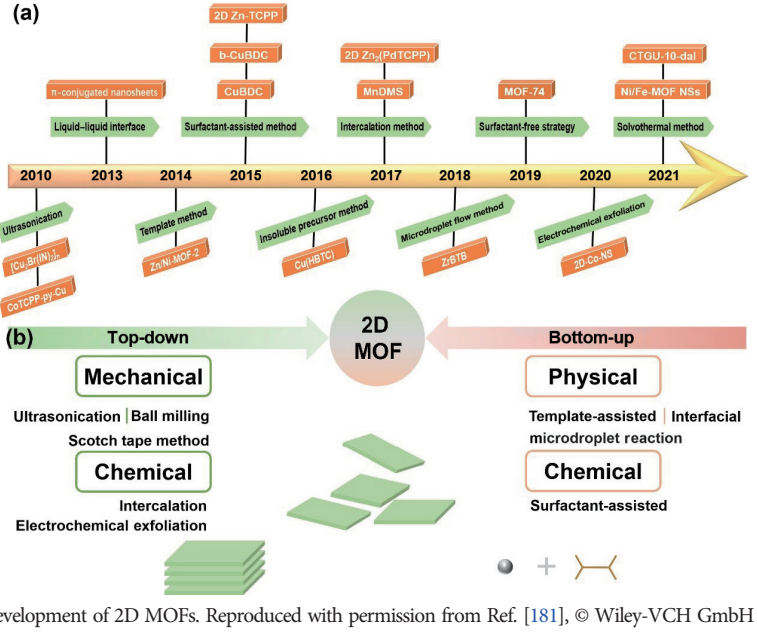

Figure 3 (a) The timeline of the development of 2D MOFs. Reproduced with permission from Ref. [181], © Wiley-VCH GmbH 2022. (b) Strategy of top-down or bottom-up synthesis of 2D MOF nanosheets.

Table 1 List of 2D MOFs synthesized by top-down and bottom-up methods

Name	Metal	Organic linker	Synthesis method	References
$[Cu_2Br(IN)_2]_n$	Cu	IN	Ultrasonication	[55]
$Cu(bpy)_2(otf)_2$	Cu	bpy, otf	Ultrasonication	[56]
Cu(1)(DMF)	Cu	H_2(1)	Ultrasonication	[57]
MOF-2	Zn	H_2BDC	Ultrasonication	[58]
$Zn_7(DMS)_6(OH)_2$	Zn	DMS	Ultrasonication	[59]
$[Co(CNS)_2(pyz)_2]_n$	Co	pyz	Ultrasonication	[60]
$Fe(Py_2th)_2$	Fe	Py_2th	Ultrasonication	[61]
NTU-9	Ti	H_2DOBDC	Ultrasonication	[62]
$Mn(DMS)\cdot H_2O$	Mn	DMS	Ultrasonication	[63]
Eu-psa	Eu	H_2PSA	Ultrasonication	[64]
$La_2(TDA)_3\cdot 2H_2O$	La	TDA	Ultrasonication	[65]
UiO-67	Hf	H_2BPDC	Ultrasonication	[66]
Cd-TPA	Cd	H_3TPA	Ultrasonication	[67]
NiFe-UMNs	Ni, Fe	TEA	Ultrasonication	[68]
CuCo-UMOFN	Cu, Co	H_2BDC	Ultrasonication	[69]
$[M_2(bdc)(dabco)]\cdot$guest	Zn, Co, Ni	H_2BDC, DABCO	Ultrasonication	[70]
ZSB-1	Zn	SBA, BPTP	Ultrasonication	[71]
$Cu(\mu\text{-}pym_2S_2)\cdot(\mu Cl)\cdot nH_2O$	Cu	pym_2S_2	Spontaneous exfoliation	[72]
MAMS-1	Ni	H_2BDC	Freezing thawing	[73]
$Zn_2(bim)_4$	Zn	bim	Ball milling	[74]
Zn_2(PdTCPP)	Zn	TCPP	Intercalation	[75]
MnDMS	Mn	DMS	Intercalation	[76]
NiCo-UMOFNs	Ni, Co	TEA	Sonochemical	[2]
Cu-TCPP	Cu	TCPP	Surfactant-assisted	[77]
PPF-3	Co	TCPP	Surfactant-assisted	[78]
NH_2-MIL-53	Al	2-ATA	Surfactant-assisted	[79]
LDH-MOF@NF	Ni, Fe	PTA	Template-assisted	[80]
$Fe_{0.1}$-Ni-MOF/NF	Ni, Fe	PTA	Template-assisted	[81]
MIL-53(FeNi)/NF	Ni, Fe	PTA	Template-assisted	[82]
ZIF-67	Co	MeIm	Template-assisted	[83]
FDM-23	Cu	m-H_2BDC	Template-assisted	[84]
Cu_3(BHT)	Cu	BHT	Interfacial	[85]
Ni-THT	Ni	THT	Interfacial	[86]
$Mo_3(HAB)_2$	Mo	HAB	Interfacial	[87]
ZBCP-MOF	Zn	bim	Interfacial	[88]

layered structure, which is beneficial to OER catalysis [53]. However, the bottom-up method can provide materials with thinner thickness and larger specific surface area, which is also beneficial to mass and electron transport [54]. Therefore, the design of synthesis method of 2D MOFs is crucial for catalyzing OER.

3.1.1 *Top-down methods*

The adjacent layers of the layered MOF are joined together by van der Waals forces, hydrogen bonds, or π–π stacking, which are much weaker than covalent bonds and coordination bonds within the layers [49]. The top-down method is to exfoliate layered bulk MOF into few layers even single layer MOF nanosheets via physical and chemical peels methods. In 2010, Zamora and co-workers fabricated 2D MOF nanosheet ($[Cu_2Br(IN)_2]_n$) by sonication exfoliation for the first time [55]. As shown in Fig. 5(a), MOF unit consisted of copper atoms, (carboxylate-bonded) isonicotinato ligands, and bromine ligand, and these units along the *bc* plane assembled a 2D square framework. These 2D layers stacked together by π–π interactions, thus forming the three-dimensional (3D) structure (Fig. 5(b)). To overcome the interlayer π–π interaction, bulk MOF was ultrasonicated about 30 min. Atomic force microscopy (AFM) images in Fig. 5(c) showed that 2D nanosheets were evenly distributed on highly oriented pyrolytic graphite (HOPG) substrates and the thickness of prepared nanosheets was about 5 Å (Fig. 5(d)), which proved the successful preparation of 2D MOF nanosheets. When preparing 2D MnDMS (DMS = 2,2-dimethylsuccinate) nanosheets by liquid ultrasonic stripping method, Cheetham and co-worker found that the solvent had a great impact on the stripping effect of MOF [63]. Among the six solvents of water, ethanol, methanol, propanol, hexane, and tetrahydrofuran, ethanol had the best stripping

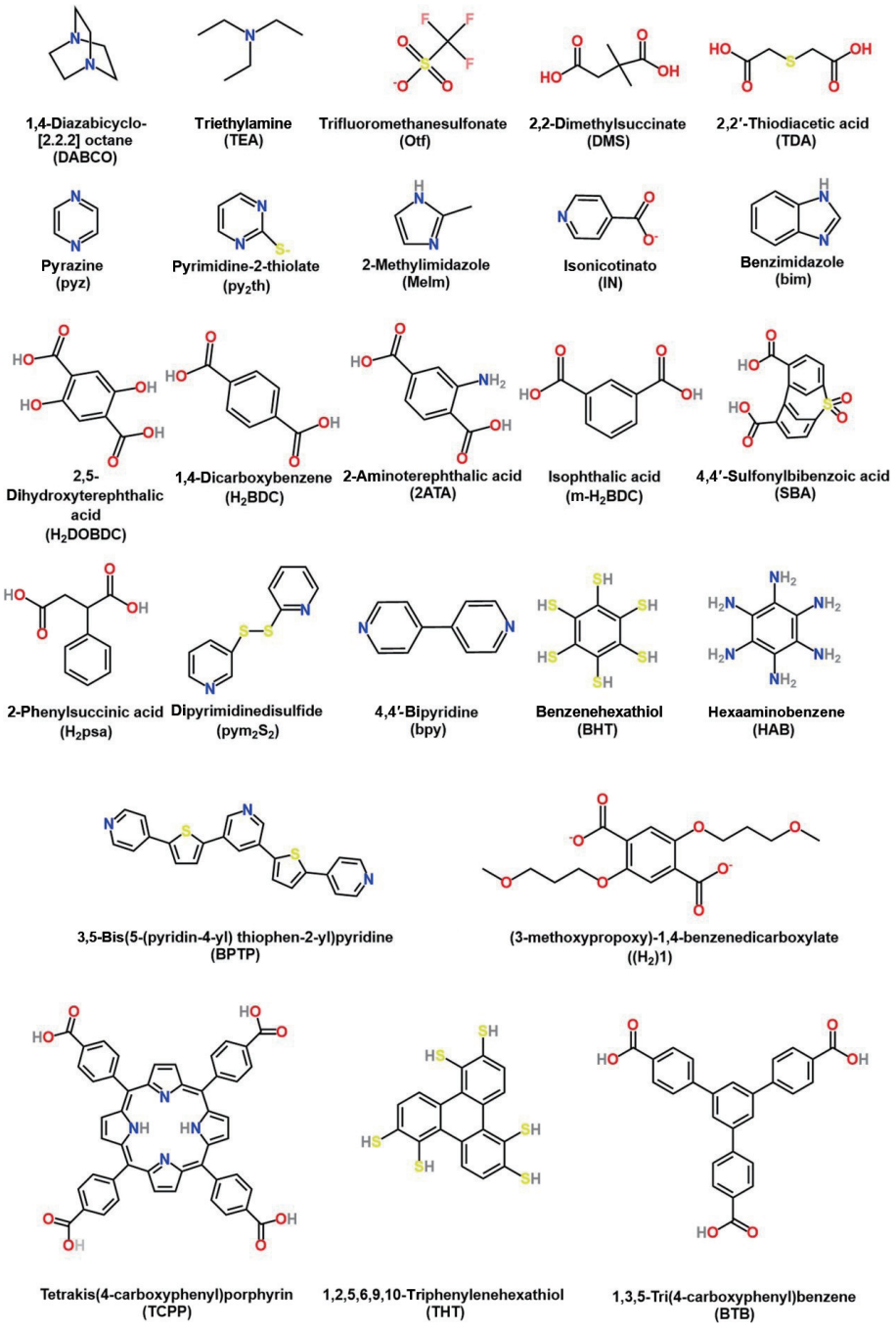

Figure 4 The organic ligand structures corresponding to Table 1.

performance. Ma et al. used different solvents (including ethanol, methanol, isopropanol, N,N-dimethylformamide (DMF), and n-hexyl alcohol) to peel ZSB-1 [71]. Experimentally, 2D ZSB-1 nanosheets can be gained only in n-hexyl alcohol. To find out the specific mechanism of solvent on MOF stripping process, molecular mechanics simulation was carried out. Calculation results (Fig. 5(e)) indicated that ZSB-1 and n-hexanol have the maximum absolute value of interaction energy (E_{int}) and van der Waals component (E_{vdW}) among these solvents, showing that n-hexanol has a strong interaction with ZSB-1. The strong interaction between solvent and MOF can weaken the interlayer force of MOF to achieve good stripping effect. Based on this, a family of single-layer MOF was prepared from 3D pillared-layer MOFs ([M_2(bdc)(dabco)]·guest (M = Zn, Co, and Ni) [70]. In general, the ultrasonic stripping method helps solvent molecules penetrate the channels of layered MOF and quickly replace the columnar ligand or destroy the interlayer force, thereby selectively destroying the interlayer bonding, achieving the effect of peeling off the layered MOF in a short time. In addition to the ultrasonic method, wet ball milling can also achieve the same purpose, but usually a combination of the two is used to achieve a better peeling effect. For example, the original $Zn_2(bim)_4$ columnar crystal was successfully peeled off into MOF nanosheets with large transverse size (1.5 μm) and ultra-thin thickness (~ 1 nm) by Peng et al. through wet ball-milling and ultrasonication [74]. Scanning electron microscopy (SEM) images clearly show that the original MOF of the cube presents a 2D nanosheet structure after soft physical peeling.

For the above-mentioned methods, solvent plays an important role for peeling process and results of layered MOF. Besides, other mechanical delamination methods, such as the scotch tape method [89], can also achieve the effect of peeling layered MOF without solvent. However, the above methods result in 2D MOF nanosheets with various thicknesses and low yields (usually < 15%) due to the low elastic modulus of most MOFs [77].

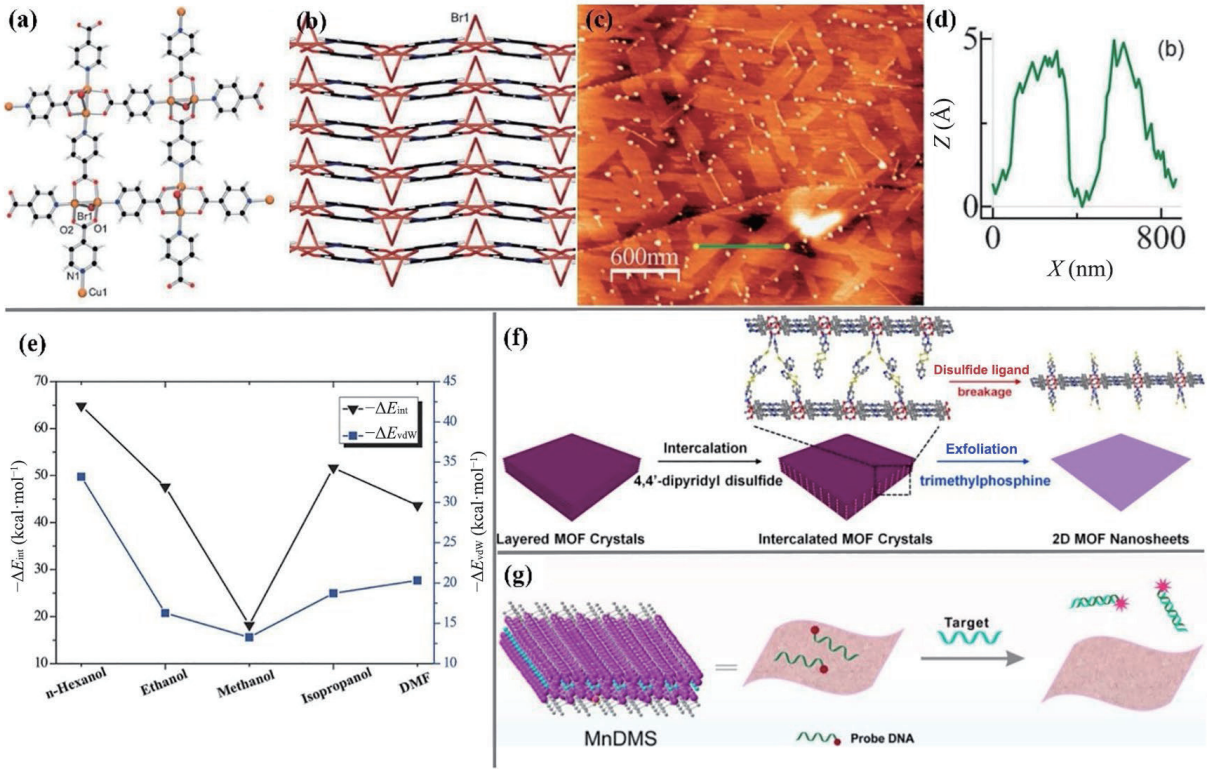

Figure 5 (a) View of single-layer $[Cu_2Br(IN)_2]_n$ nanosheet structure. (b) Stacking structure diagram along the *a* axis. (c) AFM image of flaky $[Cu_2Br(IN)_2]_n$. (d) Section height of green line in (c). Reproduced with permission from Ref. [55], © The Royal Society of Chemistry 2010. (e) E_{int} between ZSB-1 and different solvents during exfoliation and its E_{vdW} relative to that of MOF. Reproduced with permission from Ref. [71], © WILEY-VCH Verlag GmbH & Co. KGaA, Weinheim 2018. (f) Schematic diagram of 2D MOF nanosheet prepared by organic intercalation method. Reproduced with permission from Ref. [75], © American Chemical Society 2017. (g) Schematic diagram of 2D MOF nanosheet prepared by lithium i4ercalation method. Reproduced with permission from Ref. [76], © Elsevier B.V. 2017.

Electrochemical exfoliation has been shown to be an effective stripping approach to address these issues. For example, Zhou et al. used 4,4-dipyridyl disulfide (DPDS) as the embedded molecules to exfoliate Zn_2(PdTCPP) crystals [75]. As shown in Fig. 5(f), DPDS was firstly intercalated into the interlayers of MOF crystals through coordination bonding with the metal nodes, and then selectively cutting disulfide bonds by trimethylphosphine, and MOFs can be easily exfoliated into ultrathin (~ 1 nm) nanosheets with high yield (~ 57%). In addition, lithium intercalation is also an effective peeling strategy. Song et al. peeled MnDMS nanoparticles (NPs) via lithium intercalation method [76]. First, The MnDMS nanoparticles were scattered in hexane with 0.16 M n-butyllithium and stirred at room temperature for 24 h. Then, MnDMS nanoparticles embedded with lithium were centrifuged in the mixed solvent of water and ethanol to obtain MnDMS nanosheets (Fig. 5(g)). Nanosheets obtained by lithium intercalation have a smaller thickness (~ 1 nm) than those obtained by ultrasound (10–100 nm). 2D MOFs synthesized by a top-down approach generally exhibit good catalysis due to abundant surface defects arising from disruption of interlayer interactions in 3D MOF precursors. However, the drawbacks of the top-down approach, the non-uniform thickness and low yield, are still the key issues to be settled. At present, many feasible methods are also being developed, for example, the freezing thawing method proposed by Zhao et al. in stripping Ni_8(5-bbdc)$_6$(μ-Oh)$_4$ (MAMS-1), which utilizes the shear force generated by the volume change of hexane between the solid and liquid phases to peel the MAMS-1 crystal into discrete nanosheets [73].

3.1.2 *Bottom-up methods*

Different from the top-down method, the topology of the original MOFs crystal targeted by the bottom-up method can be layered or not. The bottom-up method has the advantages of high yield, controllable thickness, and large transverse size. But the key point of bottom-up strategy is to prevent MOF from growing perpendicular to the plane. Ordinary bottom-up strategies include interfacial growth methods, surfactant-assisted methods, and template-assisted methods. For the interface synthesis of MOF nanosheets, metal nodes are coordinated by organic ligands at the interface of two different phases, which limits the growth of MOF crystals in the vertical direction, resulting in the formation of MOF nanosheets. Theoretically, gas–liquid and liquid–liquid interfaces are two representative interfaces. Feng et al. fabricated a novel 2D supramolecular polymer (2DSP) sheet through the interfacial synthesis method [86]. Nanosheets were assembled at the air/water interface, as shown in Fig. 6(a), and THT monomer sub monolayer was laid on the water surface in LB trough. After the monomer was tightly compressed into a film, a solution of nickel salt was injected into the aqueous phase. With the diffusion of nickel ions to the interface and coordinated with dithiolene units, a large area of 2DSPs was formed. The lateral dimensions of 2DSPs were on the order of square millimeters, and the thickness was 0.7–0.9 nm (Fig. 6(b)). Owing to the high density and high exposure of nickel bis(dithiolene) motifs in THTNi 2DSPs, the 2D material exhibited good hydrogen evolution reaction catalytic properties. Apart from the air/water interface, the water/organic interface has also been proved to be used to synthesize 2D MOF films. For example, Wei et al. reported a $[Cu_3(C_6S_6)]$ form at the water/CH_2Cl_2 interface [85]. As shown in Fig. 6(c), Cu^{2+} (aqueous phase) and BHT (organic phase) coordinated at the interface. SEM images (Figs. 6(e)–6(g)) proved the generation of 2D Cu-BHT structure. The specific formation mechanism is shown in Fig. 6(h), BHT captured copper ions from the water/organic interface and carried them to the organic phase for assembly. Due to the interface confinement effect, the nanosheet structure was formed orderly and packed parallel to the water/CH_2Cl_2 interface. In addition to interface synthesis, template synthesis is also an efficient bottom-up approach. Zhang et al. proposed a strategy of

preparing 2D MOF with layered hydroxide as template [90]. As shown in Fig. 6(i), the metal node of hydroxide can serve as the anchor point for further growth of 2D MOF. Ni ions replaced the hydrogen atoms distributed on both sides of the flake $Co(OH)_2$, and acted as metal sites for further growth of MOF, which assembled with terephthalic acid to form MOFs. Finally, $Co(OH)_2$ was conformally converted into CoNi-MOF. SEM images (Fig. 6(j)) confirmed that CoNi-MOF completely retained the morphology of $Co(OH)_2$. Yao et al. prepared layered MOF nanoarrays using consistent tropism NiFe-LDH as templates [81], which exhibited excellent OER catalytic performance with overpotential values of 243 and 263 mV at 50 and 100 $mA·cm^{-2}$ in 1.0 M KOH, respectively. Apart from conventional preparation methods, Yang et al. studied the effect of solvent on the morphology of MOF products in detail, and found that a small amount of water and TEA could promote the growth of Fe/Co-MOF nanosheets (Fig. 6(k)) [91]. Importantly, it can be achieved that the large-scale synthesis of MOF nanosheets with a gram-scale product (approximately 2.39 g) and a yield of up to 93% through controlling solvent. Wang and co-workers prepared 2D NiFe-MOF nanosheets induced by carboxylated carbon quantum dots (CQDs-COOH) *in-situ*, and CQDs-COOH enlarged the layer spacing of the NiFe-MOF and effectively promoted the formation of NiFe-MOF nanosheets via electron-withdrawing –COOH groups [92]. The 2D MOFs fabricated by bottom-up methods have uniform thickness and high yield, but the surface properties are inhibited by relatively weak structural stability and surface additives.

3.2 Synthesis of 2D MOF derivatives

Making 2D MOF derivatives with ideal composition and structural diversity by using MOFs nanosheets as templates/precursors is one of the effective ways to solve the problems of structural stability and poor conductivity of most 2D MOFs [93–95]. At present, the most common method to prepare 2D MOF derivatives is to heat treat 2D MOF under inert/specific atmosphere and ideal temperature. For example, 2D MOF can be calcined in an inert atmosphere. With the addition of phosphorus

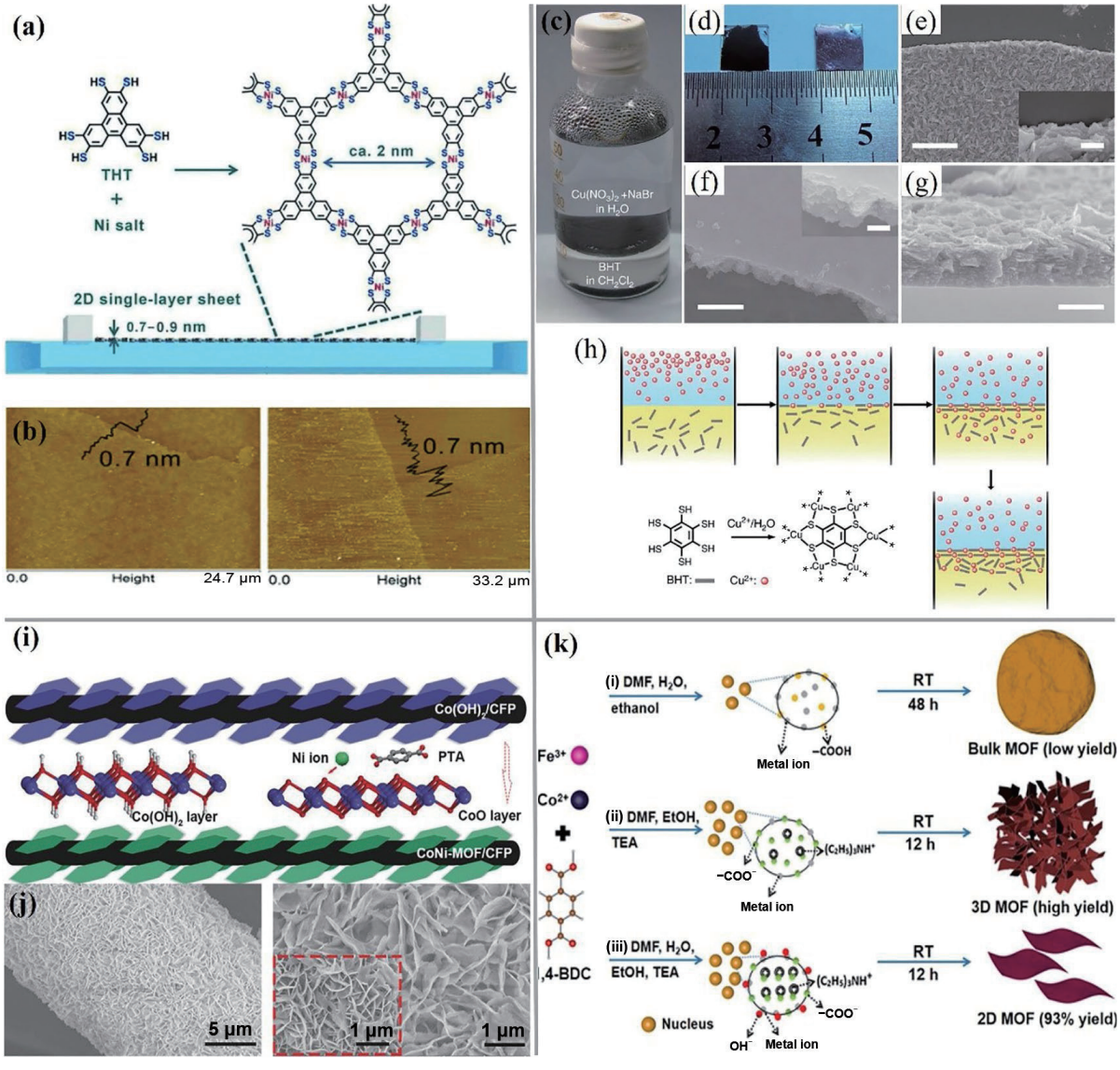

Figure 6 (a) Schematic illustration of the synthesis of 2DSP using the Langmuir–Blodgett method at the air/water interface. (b) AFM height images and corresponding cross-sectional analysis. Reproduced with permission from Ref. [86], © WILEY-VCH Verlag GmbH & Co. KGaA, Weinheim 2015. (c) Photograph of the formation of 2D Cu-BHT films at the water/organic interface. (d) Photographs of films grown on a glass substrate, upside up (right) and upside down (left). (e)–(g) SEM images of 2D films, (h) schematic diagram of the formation of films. Reproduced with permission from Ref. [85], © Macmillan Publishers Limited 2015. (i) Schematic diagram of the preparation of CoNi-MOF by template method. (j) SEM images of $Co(OH)_2$ (left) and CoNi-MOF (right). Reproduced with permission from Ref. [90], © WILEY-VCH Verlag GmbH & Co. KGaA, Weinheim 2017. (k) Schematic illustration of the synthesis of bulk, 3D, and 2D MOFs by manipulating the solvent. Reproduced with permission from Ref. [91], © Wiley-VCH GmbH 2021.

source/sulfur source/selenium source, 2D MOF can be phosphorized, sulfurized, or selenified, respectively [96]. Carbonization is also obtained by high-temperature annealing in inert atmosphere [97]. Oxidation and nitridation require direct annealing of 2D MOF precursor in air and NH_3 atmosphere [98]. If the MOF framework contains O, P, S, and other elements, it can also reduce or even not add additional oxygen/phosphorus/sulfur sources, and directly anneal in an inert atmosphere to obtain 2D MOF-derived oxides, phosphides, and sulfides. In addition, solvent heat treatment can also be used for the preparation of 2D MOF sulfide and boride.

3.2.1 *Pyrolysis*

Making derivatives of 2D MOFs by pyrolysis has high requirements for pyrolysis atmosphere, temperature, and time. For example, porous carbon for metal alloy decoration can be prepared by calcining MOF precursor at a higher temperature (above 600 °C) in an inert atmosphere. Metal phosphides, sulfides, and selenides derived from 2D MOFs can be prepared by low-temperature pyrolysis (200–600 °C) of 2D MOF under inert atmosphere and by adding phosphorus, sulfur, and selenium sources [99]. The morphology, electronic structure, and electrocatalytic performance of MOF derivatives can be adjusted by changing the pyrolysis temperature and time. For example, the MOF derivatives will maintain the microscopic morphology of the MOF precursor, but the core–shell structure may be formed by the pyrolysis of 2D MOF at a specific temperature and time, which will affect the catalytic performance of the MOF derivative for OER.

3.2.2 *Solvothermal/hydrothermal/electrochemical method*

The solvothermal/hydrothermal/electrochemical method for preparing 2D MOF derivatives takes advantage of the instability of MOF in solution. Under the action of solvent, MOF will begin to recombine at a specific temperature to form other substances. For example, if the solution contains sulfur, phosphorus, and boron, MOF will be derived into corresponding sulfide, phosphide, or boride. In addition, hydroxide is also a common product after hydrothermal/electrochemical treatment [100].

The purpose of converting 2D MOF into 2D MOF derivatives by reasonable means is to improve the conductivity and stability of the material and to improve its catalytic properties. In addition to the methods mentioned above, combining 2D MOFs with metal particles/clusters, metal oxides/sulfides, etc., or combining 2D MOFs with other two-dimensional materials is an effective means to construct MOF derivatives [101]. Therefore, in the process of studying 2D MOF materials as (pre)catalytic materials, it is also necessary to study the post-treatment methods.

3.3 Characterization of materials

Characterization of 2D MOFs is crucial for developing the functionality of these materials and expanding new 2D MOFs synthesis strategies. The characterization of 2D MOFs usually includes (1) phase structure, (2) thickness, (3) stability, and (4) pore size. Most characterization techniques of block MOFs can conduct structural analysis on 2D MOFs without major modification, but more accurate data was needed to the characterization of 2D MOFs.

Electron microscopy technology is the most intuitive and more general technology for analyzing 2D morphology, including SEM, transmission electron microscopy (TEM), scanning TEM (STEM), etc. SEM can evaluate the delamination state of the sample and the possibility of falling off (Figs. 7(a) and 7(b)). TEM can observe the geometric shape and layered configuration of particles (Fig. 7(c)). STEM can observe the particle arrangement rule of the material (Fig. 7(d)). In addition, SEM or TEM can also provide the element distribution on the sample surface combining with energy-dispersive X-ray spectroscopy (EDS).

Even though the 2D morphology of the material has been clearly observed, X-ray diffraction (XRD) is also needed to prove the atomic arrangement in the MOF nanosheet. Due to the size limitation, the crystal data of 2D MOF cannot be obtained by single crystal XRD (SC-XRD) like bulk MOFs. Therefore, 2D MOFs are often characterized by powder XRD (PXRD). Powder X-ray diffraction can evaluate the crystallinity, phase, and crystal plane spacing of samples. But these results are a statistical average and cannot represent the structure of single MOF crystal. Therefore, it is necessary to refer to the known crystal structure. For MOFs, Brunauer–Emmett–Teller (BET) is a very important characterization technology. By measuring the gas adsorption data and fitting the gas adsorption–desorption isotherm of 2D MOFs, BET can detect their pore structure and calculate the specific surface area of two-dimensional MOFs.

To identify the element composition of the surface and the coordination of the metal connector, it is necessary to characterize 2D MOFs by X-ray photoelectron spectroscopy (XPS). However, XPS is surface technology that only detects the outermost layer of materials, so other characterization methods that provide chemical information need to be considered, such as fourier transform infrared (FTIR), Raman, and solid-state nuclear magnetic resonance (NMR) spectroscopy.

4 2D MOFs and their derivatives for catalyzing OER

4.1 2D MOFs for catalyzing OER

In recent years, 2D transition metal (cobalt, nickel, copper, and iron-based) MOFs have been directly used as efficient catalysts for OER, as shown in Table 2. Here, we introduce several ligands for the synthesis of 2D MOFs, including terephthalic acids-like ligands and π-conjugated ligands such as hexaiminotriphenyl, hexaaminobenzene (HAB), and phthalocyanine. 2D MOFs synthesized with these ligands have shown high-efficient catalytic OER performance.

4.1.1 *Carboxylic acid ligands*

When carboxylic acid ligands (especially para-position carboxyl functional groups, such as H_2BDC, DHBDC, and NH_2-BDC) coordinate with metal ions, each metal ion links with six oxygen atoms from the solvent or carboxyl, forming an octahedral unit. These octahedral edges and corners are connected to form a layered structure, which has abundant unsaturated sites and has been proved to highly active for OER. Taking an example of H_2BDC, Tang et al. synthesized Ni-UMOFN, Co-UMOFN, and NiCo-UMOFN using H_2BDC [2], which were composed of H_2BDC linked with Co and Ni ions and AFM image showed that the thickness of NiCo-UMOFN was about 3.1 nm for NiCo-UMOFN, corresponding to four metal coordination layers or three coordination structure layers. Due to the termination of the coordination bond between H_2BDC and the surface metal atom, the ultra-thin NiCo-UMOFN produced massive unsaturated metal sites on the surface, hence NiCo-UMOFN exhibited the excellent OER catalytic activity (250 mV at 10 mA·cm^{-2} on glassy carbon electrode or 189 mV on copper foam electrode). *In situ* X-ray absorption spectroscopy (XAS) confirmed that the Co and Ni sites in NiCo-UMOFN were more active than those in bulk MOF, which were more easily oxidized to high valence states to enhance catalytic performance. Density functional theory (DFT) calculation results indicated that the coordination unsaturated metal atoms provided the main active sites and the ultra-thin 2D

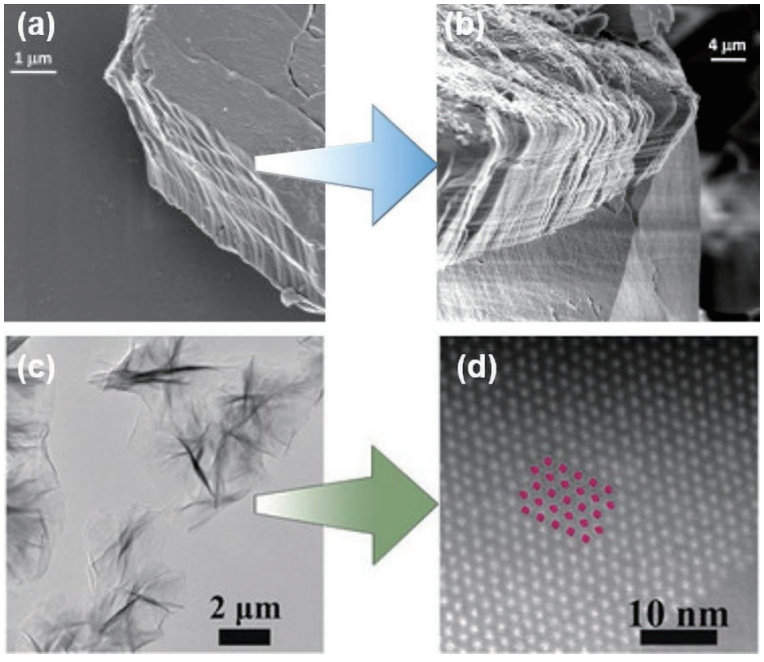

Figure 7 (a) SEM image of bulk-type CuBDC MOF crystals. (b) SEM image of CuBDC MOF nanosheets. Reproduced with permission from Ref. [182], © Macmillan Publishers Limited 2014. (c) TEM image of $Hf_6O_4(OH)_4(HCO_2)_6(BTB)_3$ nanosheets. (d) HAADF image of the $Hf_6O_4(OH)_4(HCO_2)_6(BTB)_3$ nanosheets. Reproduced with permission from Ref. [183], © WILEY-VCH Verlag GmbH & Co. KGaA, Weinheim 2016.

Table 2 OER activity of reported 2D MOFs electrocatalysts in 1.0 M KOH

Catalyst	Overpotential (η_{10})	Tafel slope	Stability	References
Co-CuTCPP	396 mV	58 mV·dec^{-1}	10 h	[102]
CoFe-MOF	355 mV	49.05 mV·dec^{-1}	15 h	[103]
(Co, 0.3Ni)-HMT	330 mV	66 mV·dec^{-1}	20 h	[104]
Co-Ni@HPA-MOF	320 mV	58 mV·dec^{-1}	—	[105]
FeCo-MNS-1.0	298 mV	21.6 mV·dec^{-1}	14 h	[106]
NiCo-LDH@MOFs-4 h	289 mV	55.2 mV·dec^{-1}	300 h	[107]
Co_3Fe-MOF	280 mV	38 mV·dec^{-1}	10 h	[108]
(U+S)-CoFe-MOF	277 mV	31 mV·dec^{-1}	1 h	[109]
Co-MOF/NF	270 mV	75 mV·dec^{-1}	30 h	[110]
Ni/Co-MOF/NF	270 mV (η_{50})	35.4 mV·dec^{-1}	8 h	[111]
NiFe MOF/NF	270 mV (η_{50})	55 mV·dec^{-1}	20 h	[112]
Ni-MOF@Fe-MOF	265 mV	82 mV·dec^{-1}	—	[113]
CoNi-MOF (Co:Ni = 1:1)	265 mV	56 mV·dec^{-1}	12 h	[114]
Fe-Ni MOF NSs/NF	258 mV (η_{50})	40.8 mV·dec^{-1}	24 h	[115]
$Ni_{0.5}Co_{1.5}$-bpy(PyM)	256 mV	81.8 mV·dec^{-1}	8 h	[116]
Co_3(HITP)$_2$	254 mV	86.5 mV·dec^{-1}	12 h	[117]
$FeCo_2$ Ni-MOF-74	254 mV	21.4 mV·dec^{-1}	100 h	[118]
NiFe-MOF NSs	240 mV	73.44 mV·dec^{-1}	16 h	[54]
Cu-Fe-NH_2 MOF	238 mV	60.8 mV·dec^{-1}	24 h	[119]
MOF-Fe/Co(1:2)	238 mV	52 mV·dec^{-1}	14 h	[91]
S-CoFe-PBA/CFP	235 mV	35.2 mV·dec^{-1}	24 h	[120]
NiFe-MOF/FF-0.5	216 mV (η_{50})	73.4 mV·dec^{-1}	50 h	[121]

structure exposed more active sites. The coordination between different metals finetuned the electronic structure of materials and optimized the adsorption barrier of each metal. In addition, Huang et al. reported a Ni-Fe-MOF nanosheets. And AFM images (Fig. 8(a)) showed that the thickness of nanosheets is from 1.67 to 2.58 nm, corresponding to two to three coordination structure layers (Fig. 8(b)) [122]. Compared to Ni-MOF NSs (386 mV) and Fe-MOF NSs (no OER activity), Ni-Fe MOF NSs showed more excellent OER catalytic activity with overpotential of 221 mV at 10 mA·cm^{-2}. XPS and DFT results revealed the origin of excellent OER catalytic activity of Ni-Fe-MOF NSs. As shown in Figs. 8(c) and 8(d), the Ni 2p and Fe 2p peaks of the Ni-Fe-MOF NSs shifted to a higher binding energy than single metal MOF, meaning strong electronic interactions in Ni-Fe-MOF NSs.

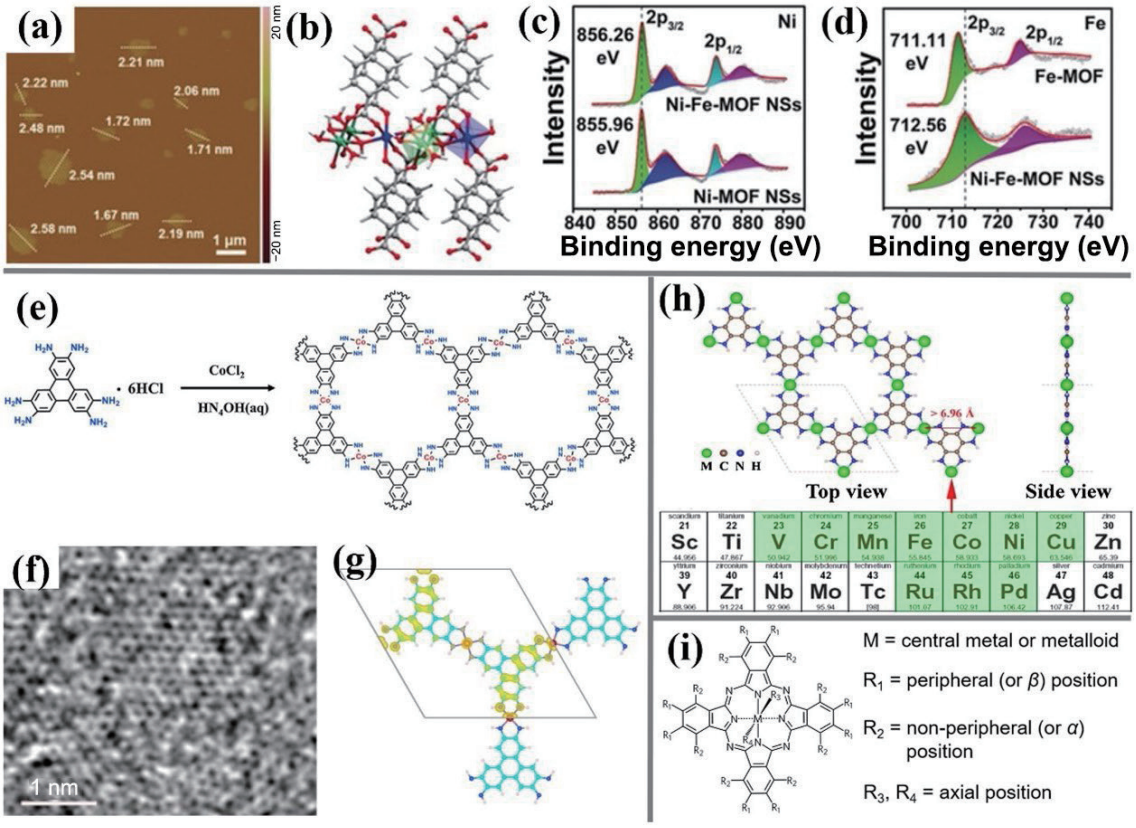

Figure 8 (a) AFM image of Ni-Fe-MOF NSs. (b) Crystal structure of Ni-Fe-MOF NSs, the XPS spectra of Fe-MOF, and Ni-Fe-MOF NSs of (c) Ni 2p and (d) Fe 2p. Reproduced with permission from Ref. [122], © WILEY-VCH Verlag GmbH & Co. KGaA, Weinheim 2019. (e) Schematic diagram of the structure and preparation of $Co_3(HITP)_2$. (f) HRTEM image of $Co_3(HITP)_2$. (g) The charge density distribution of $Co_3(HITP)_2$,Reproduced with permission from Ref. [117], © Elsevier B.V. 2020. (h) Structure of 2D hexaaminophenyl coordination polymers. Reproduced with permission from Ref. [184], © Elsevier Inc. 2017. (i) Schematic diagram of the structure of phthalocyanine. Reproduced with permission from Ref. [130], © The Royal Society of Chemistry 2021.

Furthermore, DFT results revealed that the low OER overpotential comes from the substitution of Fe at the Ni site, which reduced the potential barrier for the formation of *OH. Except H_2BDC, using other ligands such as DHBDC and NH_2-BDC can also form MOF nanosheets, and the product exposes intrinsic OER activity on their own or as precursor materials. On the other hand, it has been reported that the surface changes irreversibly after OER, which may produce new active sites. For example, the material surface changes into hydroxide oxide during the OER process, which greatly challenges the validity and accuracy of theoretical simulation. We will discuss in detail the effect of this surface change on OER activity in the next section. In a word, the layered MOF constructed by carboxylic acid ligands has great catalytic potential for OER. However, more advanced ways are needed to detect and monitor the surface changes of materials during the OER process to judge the accurate active centers of materials and establish an accurate OER reaction path.

4.1.2 *π-conjugated ligands*

In general, poor conductivity is a limiting factor affecting the development of MOFs as an effective electrocatalyst, thus, improving conductivity can help MOFs effectively enhance the electrocatalytic activity. Constructing graphene-analogous π-d conjugated MOFs with π-conjugated ligands and metal nodes is one of the effective ways to improve the conductivity of MOFs [123–125]. π-conjugated ligand is a typical ligand for forming 2D MOFs, and the nanosheets possess a special structure in which each of the metallic ions is coordinated with multiple heteroatoms (such as nitrogen and sulfur atoms). Interestingly, such TM-X_n structure has been proved to great electrocatalytic potential for OER. Taking $Co_3(HITP)_2$ synthesized by Huang et al. as an example, it consists of Co atoms coordinated with HITP (Fig. 8(e)), and has superior OER electrocatalytic activity than commercial RuO_2 and IrO_2 [117]. High-resolution TEM (HRTEM) image (Fig. 8(f)) clearly showed hexagonal pores like a honeycomb pattern. Meanwhile, X-ray absorption near edge structure (XANES) profile of $Co_3(HITP)_2$ proved that the Co exists in the form of CoN_4. All of these indicated $Co_3(HITP)_2$ have lots of CoN_4 moieties and possess good conductivity, which is the reason why $Co_3(HITP)_2$ has good OER catalytic activity. In addition, DFT calculation results also showed that $Co_3(HITP)_2$ has typical π-conjugation characteristics, since the projected density of states (PDOS) near the Fermi level is almost completely contributed by p_z orbitals of C, p_z orbitals of N, and delocalized d_{xz} and d_{yz} orbitals of Co, and the frontier orbitals of $Co_3(HITP)_2$ are greatly delocalized in the whole plane (Fig. 8(g)). Similarly, Liu et al. prepared 2D $Ni_3(HITP)_2$ films with a thickness of about 5 nm by interface synthesis [126]. Due to its large pore size and high density of Ni-N_x motifs, 2D $Ni_3(HITP)_2$ films showed outstanding OER performance. At the current density of 10 mA·cm^{-2}, the voltage of $Ni_3(HITP)_2$ is 1.62 V, which is 20 mV lower than that of commercial IrO_2 catalyst. Zhao et al. systematically studied the electrocatalytic activity of $TM_3(HITP)_2$ with transition metal (Fe, Co, Ni, Cu, and Zn) by DFT [127]. The calculation results showed that for $Ni_3(HITP)_2$, $Cu_3(HITP)_2$, and $Zn_3(HITP)_2$ monolayers, intermediates were more likely to be adsorbed on the top of C atom, while for $Fe_3(HITP)_2$ and $Co_3(HITP)_2$ monolayers, the top of TM atoms was the preferred adsorption sites in adsorption energy. It was worth noting that the formation of OOH* (the third step) was a potential limiting step in the whole OER process. The η values of $TM_3(HITP)_2$ (TM = Fe, Co, Ni, Cu, and Zn) were 0.83, 0.36, 0.73, 0.75, and 0.89 V, respectively, which indicated that these

$TM_3(HITP)_2$ monolayers had high OER catalytic activity. Especially, the overpotential of $Co_3(HITP)_2$ monolayer was even lower than that of the most famous OER catalyst IrO_2 (η = 0.42 V). In addition to HITP, as the smallest π-conjugated ligands, HAB also shows high conductivity and good catalytic activity in the honeycomb 2D lattice of MOFs. As shown in Fig. 8(h), in the unit cell of 2D HAB-MOF, each transition metal atom is coordinated by four N atoms to form a square plane arrangement of nitrogen linked metal macrocycles. Wang et al. synthesized Co-HAB MOFs with different morphologies and found that compared with nanoparticles and bulk Co-HABs, layered MOFs (average thickness = 4.5 nm) had the best OER catalytic activity with the overpotential of 310 mV at 10 $mA{\cdot}cm^{-2}$ in 1.0 M KOH solution [128]. DFT calculation results revealed that the OER overpotential at C site is lower than that at Co site, indicating higher catalytic activity for C atom in the conjugated ring. Later, they reported a self-supporting electrode with a layered structure ($CoNi$-HAB/$Co(OH)_2$/CFP) (CFP = carbon fiber paper) [129], which has larger interlayer space than $Co(OH)_2$ to accelerate mass transfer. Benefiting from the π-d conjugated network combined with layered 2D $Co(OH)_2$, $CoNi$-HAB/$Co(OH)_2$/CFP exhibited excellent catalytic performance with a low overpotential (219 mV) and Tafel slope (42 $mV{\cdot}dec^{-1}$). DFT calculations also confirmed that bimetallic $CoNi_2HAB_2$ promoted good adsorption of OER intermediates and enhanced OER performance. Furthermore, phthalocyanines (Pcs), composed of four isoindole subunits with 18 π electrons, are synthetic analogues of naturally occurring porphyrins with π-conjugated structure. Due to the unsaturated low coordination environment in which the central metal ion coordinates with four isoindole subunits, porphyrin complexes such as phthalocyanine have excellent catalytic activity (Fig. 8(i)) [130]. Du et al. selected Pc unit as organic ligand and constructed π-conjugated 2D NiPc-MOF by bottom-up method [131]. The NiPc-MOF sedimented on FTO exhibited good catalytic OER activity, which had low onset potential (< 1.48 V, overpotential < 0.25 V) and high mass activity (883.3 $A{\cdot}g^{-1}$).

4.1.3 *Other ligands*

As another kind of MOF with TM-X_n structure, these MOFs constructed by imidazole ligands and tetrahedral coordination metals do not have conductivity like π-d conjugated MOF, but their ability to catalyze OER has also been confirmed. For example, Jayaramulu et al. prepared Co-ZIF-9(III) (ZIF = zeolitic imidazolate framework) nanosheets by liquid phase ultrasonic stripping of columnar layered Co-ZIF-9 [132]. The experimental data showed that the active site of the nanosheet was Co-N_4 structure, N_4-COOH was formed during the OER catalytic process, and the mechanism was similar as Co-porphyrin and related systems. In another example, Xu et al. substituted the iron oxide cluster (Fe_{28}) for the iron in the 2D zeolite imidazolite framework, and obtained 2D ZIF-L@Fe_{28} [133]. The experimental data showed that ZIF-L@Fe_{28} has excellent OER catalytic activity and stability. At 10 $mA{\cdot}cm^{-2}$, the overvoltage was 312 mV and the Tafel slope was 78 $mV{\cdot}dec^{-1}$, which were better than ZIF-67@Fe_{28}, the pristine 2D ZIF-L, and 3D ZIF-67. The experimental results showed that the bidirectional synergistic effect between Fe_{28} and ZIF and the etching effect of Fe_{28} on ZIF-L in aqueous solution improve the catalytic ability of the material.

4.2 2D MOF derivatives for catalyzing

Although the OER catalyzed by 2D MOFs has been deeply studied, the shortcomings of MOF (poor stability and conductivity) limit its further improvement. In addition to developing conductive MOFs with higher catalytic activity, obtaining MOF derivatives through post-treatment is an effective method to improve its OER catalytic performance [134–136]. Based on inheriting the ultra-thin morphology and the abundant active sites of 2D MOF precursor, 2D MOF derivatives exhibit faster electronic transmission and mass transfer capability, promoting reaction kinetics [137]. In addition, the carbon skeleton of organic ligands and S, P, and Se introduced by post-processing can improve the conductivity of materials and realize rapid electron transfer [45, 138]. More importantly, compared with the unstable coordination bond in MOF, the stable chemical bond in the derivative can improve the stability of materials in extreme environments. Table 3 provides a detailed evaluation of 2D MOF derivatives in recent years [139–161].

4.2.1 *Metal (oxy)hydroxide*

The evolution of 2D MOFs into layered hydroxides requires two processes: substitution of the hydroxyl ions and the bond breaking between the organic ligands and the hydroxide layers. The former process is the conversion of MOF to metal hydroxide-organic framework (MHOFs), the latter process is the exfoliation of metal hydroxide-organic frameworks, and the both products have good OER catalytic performance [141, 145]. As mentioned earlier, MOF surface may change into hydroxides irreversibly during the catalytic OER process [162, 163]. Taking an example of CoNi-MOFNA reported by Dong et al., extended X-ray absorption fine structure (EXAFS) results showed that the coordination number of Co and Ni atoms is about 5.8, which proved the intrinsic active sites are unsaturated MO_5 on surface [100]. However, MOF surface was partially dissolved to form hydroxyl oxides, and ultra-fine metal hydroxyl oxide clusters are separated by MOF nanosheets after 1000 CV cycles. The composite of MOOH and MOF retained the catalytic activity, and further improved the stability of the material. This transformation occurs not only in the OER reaction process, but also in the synthesis of MOF materials. For instance, Cai et al. realized the transformation of ZIF-9 from 3D to 2D structure by adjusting the proportion of reaction solvent (water and ethanol), and simultaneously generated ZIF-9(III)/Co LDH nanocomposites (Fig. 9(a)) [145]. Due to the thinner structure and the interface interaction between LDH and MOF, ZIF-9(III)/Co LDH-15 emerged better OER performance than Co LDH and bulk ZIF-9(III) (Fig. 9(b)). The stability test and the characterization images before and after OER also exhibited that the catalyst had advanced stability. As shown in Figs. 9(c)–9(f), theoretical calculation showed that the free energy change value of ZIF-9(III)/Co LDH in the speed limit step was 2.19 eV, which was significantly lower than that of ZIF-9(III) (3.3 eV) and Co LDH (2.56 eV). Such uncomplicated conversion greatly improved the number of active sites and stability of the material. To better understand the catalytic mechanism and performance of HMOFs for OER, Yuan and colleagues designed a series of HMOFs composed of layered hydroxides and aromatic carboxylic acid ligands, and explored their chemical stability and OER activity [164]. Leaching percentage of linkers indicated that $Ni_2(OH)_2(L_4)$ had the best stability due to the more powerful π–π interaction between the organic ligands of $Ni_2(OH)_2(L_4)$. Taking $Ni_2(OH)_2(L_4)$ as the research object, the experimental results showed that the introduction of acidic metals can positively shift the redox potential of Ni (in the order of $La^{3+} < Zn^{2+} < Y^{3+} < Al^{3+} < Sc^{3+} < Fe^{3+}$), and the steady-state OER overpotential decreases linearly with the increase of Ni redox potential. Among them, Fe/$Ni_2(OH)_2(L_4)$ showed the best OER catalytic performance. In general, whether it is the transformation of the surface or that of the whole material maybe greatly improve the OER catalytic performance. First, the stability of the material is improved after transformation. Second, the formation of metal hydroxides and the subsequent *in situ* oxidation of MOOH species play a crucial role in the OER process. Third, more unsaturated active sites are

Table 3 OER activity of reported 2D MOF-derived electrocatalysts in 1.0 M KOH

Catalyst	Overpotential (η_{10})	Tafel slope	Stability	References
Co@N-carbon-800	560 mV (η_{100})	61.0 mV·dec^{-1}	—	[139]
NiFeZn-MNS/NF	350 mV (η_{50})	49.0 mV·dec^{-1}	120 h	[140]
CoNi hydroxide UNSs	324 mV	37.2 mV·dec^{-1}	3 h	[141]
MOF-D $CoSe_2$	320 mV	60.0 mV·dec^{-1}	—	[27]
CoP/NF	317 mV (η_{50})	65.6 mV·dec^{-1}	12 h	[142]
Co-MOF/H_2	312 mV	89.7 mV·dec^{-1}	40 h	[143]
HXP@NC800	307 mV	48.0 mV·dec^{-1}	8 h	[97]
FeCo-MOF-EH	301 mV	42.0 mV·dec^{-1}	30 h	[144]
ZIF-9(III)/Co LDH-15	297 mV	65.0 mV·dec^{-1}	15 h	[145]
CoP-NS/C	292 mV	64.0 mV·dec^{-1}	24 h	[96]
Mn-CoP	290 mV	76.0 mV·dec^{-1}	20 h	[146]
CoP_x@CNS	286 mV (η_{50})	70.0 mV·dec^{-1}	60 h	[26]
Py-1@SNC600	284 mV	56.0 mV·dec^{-1}	8 h	[147]
Ni@NC-800	280 mV	45.0 mV·dec^{-1}	10 h	[148]
CoFeBiP	273 mV	77.3 mV·dec^{-1}	25 h	[149]
Ni-Co-S HPNA	270 mV	80.0 mV·dec^{-1}	12 h	[150]
Ir-Ni-NS-2	270 mV	70.0 mV·dec^{-1}	—	[151]
$Co_{0.7}Fe_{0.3}P$/C	270 mV	27.0 mV·dec^{-1}	—	[93]
CoS_2/CoS	269 mV	52.0 mV·dec^{-1}	—	[94]
CoNiFe LTHs	262 mV	88.1 mV·dec^{-1}	50 h	[152]
CoSe/$MoSe_2$	262 mV	54.9 mV·dec^{-1}	10 h	[99]
Am-$FeCo(OH)_x$-30	257 mV	47.0 mV·dec^{-1}	16 h	[153]
Ni-MOF-250	250 mV (η_{50})	88.6 mV·dec^{-1}	20 h	[95]
$FeCo_{0.5}Ni_{0.5}$-LDH	248 mV	38.0 mV·dec^{-1}	50 h	[154]
Ni@CoO@Co-MOFC	247 mV	51.0 mV·dec^{-1}	24 h	[155]
NiCo/Fe_3O_4/MOF-74	238 mV	29.0 mV·dec^{-1}	36 h	[156]
CoNiP/NF	234 mV	47.0 mV·dec^{-1}	20 h	[157]
$FeNi_3$-Fe_3O_4 NPs/MOF-CNT	234 mV	37.0 mV·dec^{-1}	20 h	[98]
NiFe-MS/MOF@NF	230 mV (η_{50})	32.0 mV·dec^{-1}	17 h	[158]
NiCoZnP/NC	228 mV	60.1 mV·dec^{-1}	45 h	[159]
NiFe-MOF/$NiSe_x$/NF	198 mV	30.6 mV·dec^{-1}	40 h	[160]
CC-NC-NiFeP	145 mV	47.0 mV·dec^{-1}	18 h	[161]

fully exposed with the separation of organic ligands and metal hydroxide layers [165, 166]. Taking an example of Co MOF (CoHKUST-1) prepared by Qian et al., due to the metastable nature of the Co–O coordination bonds, MOF gradually degraded in alkaline solution [167]. The experimental results showed that the OER catalytic performance of Co-MOF could be greatly reduced when the OER test is performed continuously (η_{10} gradually increases from 310 mV, and its η_{10} value has increased to 340 mV in the fifth LSV test). MOF fully converted (oxy)hydroxide has low resistance and the high C_{dl} value and exhibits better electrochemical performance for a long time in 1.0 M KOH solution than Co-MOF, in which η_{10} value increases by only 7 mV. Except MOFs composed of single metal are converted to hydroxide, multi-metal hydroxide is also an effective mean to improve OER catalytic activity [141, 145, 153, 168]. For example, Ding et al. prepared CoM (M = Ni and Zn) ultrathin nanosheets by MOF-mediated method [141]. Compared with Co hydroxide nanosheets, CoNi hydroxide nanosheets exhibited better catalytic activity with the overpotential of 372 mV at the current density of 100 mA·cm^{-2}, which is superior than Co hydroxide nanosheets (401 mV) and IrO_2 (465 mV). Du et al. synthesized 2D CoNiFe LTHs with higher OER catalytic activity using the same method [152]. The research showed that the introduction of Fe could change the electronic structure of CoNi based hydroxide and enhance its electronic conductivity to achieve rapid electron transport. Similarly, Jia et al. synthesized a hybrid composed of amino-functionalized iron-based MOF and $FeCo(OH)_x$ nanosheets [153]. At the current density of 10 mA·cm^{-2}, the overpotential of $FeCo(OH)_x$ nanosheets was as low as 257 mV. Gu and co-workers used a series of MOFs ($FeCo_xNi_{1-x}$-MOF) grown on copper foil to synthesize LDH in 1.0 M KOH for 30 min [154]. The derived $FeCo_{0.5}Ni_{0.5}$-LDH shows an ultrathin hierarchical nanosheets structure and exhibits superior OER catalytic activity with a low overpotential of 248 mV at 10 mA·cm^{-2} and long-term catalytic stability over 50 h. The Raman spectra of $FeCo_{0.5}Ni_{0.5}$-LDH indicated that the OER active sites were NiOOH. Besides, electron paramagnetic resonance (EPR) spectroscopy indicated a modulating effect of Co cation on the electronic structure of FeNi-LDH. 2D MOF-derived metal hydroxides have attracted increasing interest for OER electrocatalysis because of high

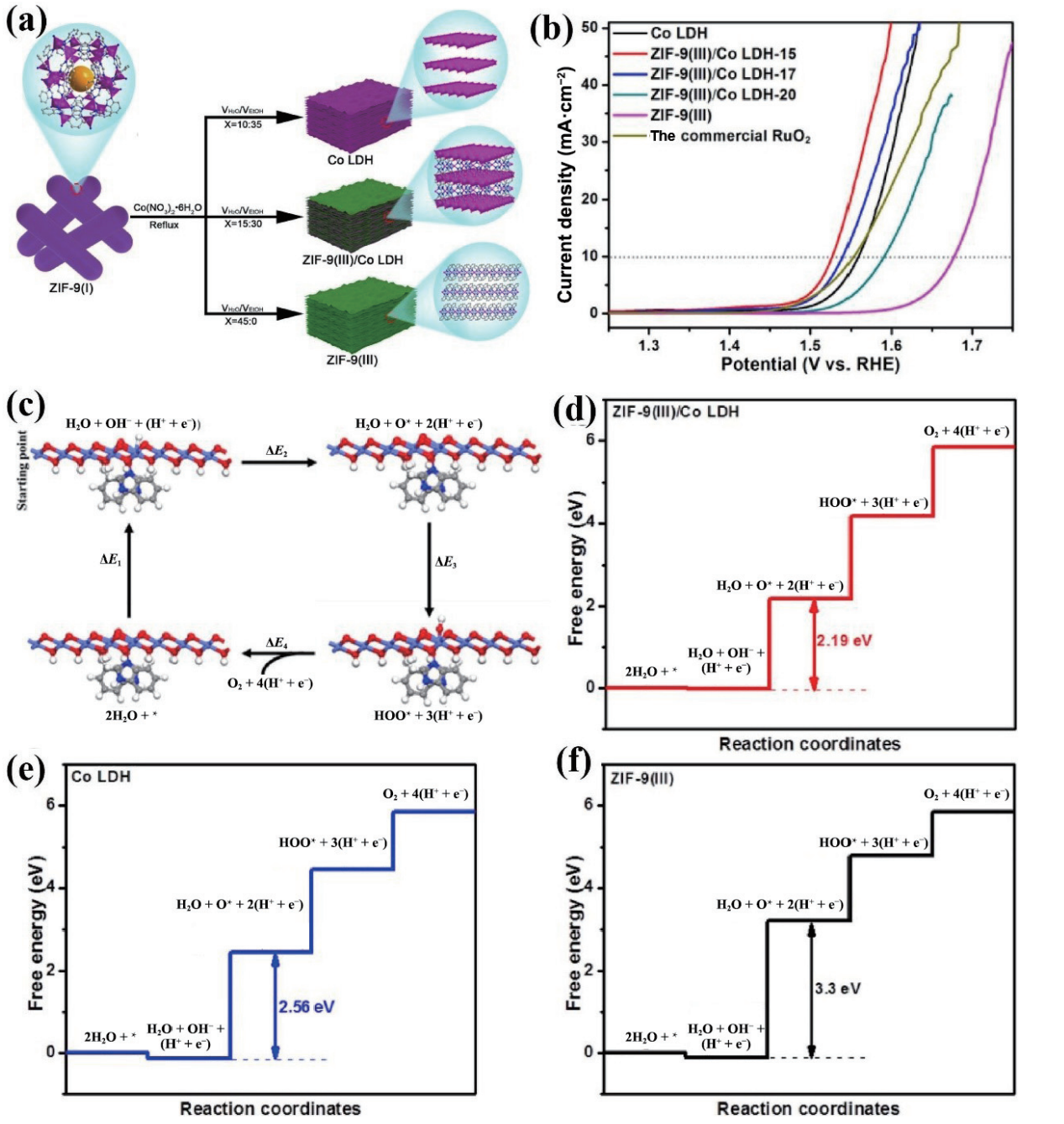

Figure 9 (a) Schematic illustration of solvent-controlled synthesis of Co LDH, ZIF-9(III)/Co LDH, and ZIF-9(III). (b) LSV curves of prepared samples. (c) Schematic diagram of OER mechanism on ZIF-9(III)/Co LDH. (d) OER Gibbs free energy diagram of ZIF-9(III)/Co LDH. (e) OER Gibbs free energy diagram of Co LDH, and (f) OER Gibbs free energy diagram of ZIF–9(III). Reproduced with permission from Ref. [145], © Elsevier B.V. 2021.

performance and easy preparation, but further comprehensive research on the OER catalytic mechanism of MOF composite hydroxide is needed, as shown earlier.

4.2.2 *Metal/alloys/oxides*

2D MOFs can form carbon supported metal/alloy/oxides nanostructures during pyrolysis. Metal/alloy/oxides nanostructures and carbon layers generated by metal units and organic ligands in 2D MOFs ensure the number of active centers and high conductivity of OER [98, 139, 148, 155]. As for 2D MOF linked by oxygen-containing functional group, metal and oxygen could form metal oxide and the basic carbon skeleton could be maintained at relatively low annealing temperatures (200–600 °C). But when the linking group is not an oxygen-containing functional group or the temperature exceeds 600 °C, the basic skeleton of MOF would be destroyed, and the pyrolysis product would be carbon supported metal/alloy nanostructures. 2D MOF-derived metals [97, 139, 148, 169], alloys [23, 170], oxides [24, 95, 171, 172], and hybrid metal oxides [98, 143, 155] encapsulated in carbon nanostructures are attracting growing attention. For instance, Xu et al. synthesized a material (Ni@NC) of nitrogen doped graphene carrying Ni NPs by high-temperature (600–900 °C) pyrolysis of Ni-MOFs in nitrogen atmosphere (Fig. 10(a)) [148]. The characterization results revealed that Ni-MOFs were 2D nanosheets with a transverse size of 500–800 nm, and carbonization products (Ni@NC) were spherical nanostructures with a diameter of 20–30 nm. As shown in Figs. 10(b) and 10(c), Ni@NC-800 had an optimal overpotential of 280 mV at 10 mA·cm^{-2} and catalytic stability over 10 h. In addition, a 2D Co@N-carbon nanocomposite was obtained by Xu et al. through high-temperature annealing of Co-HPA MOF nanosheet [139]. Co@N-carbon-800 can reach 100 mA·cm^{-2} current density at the

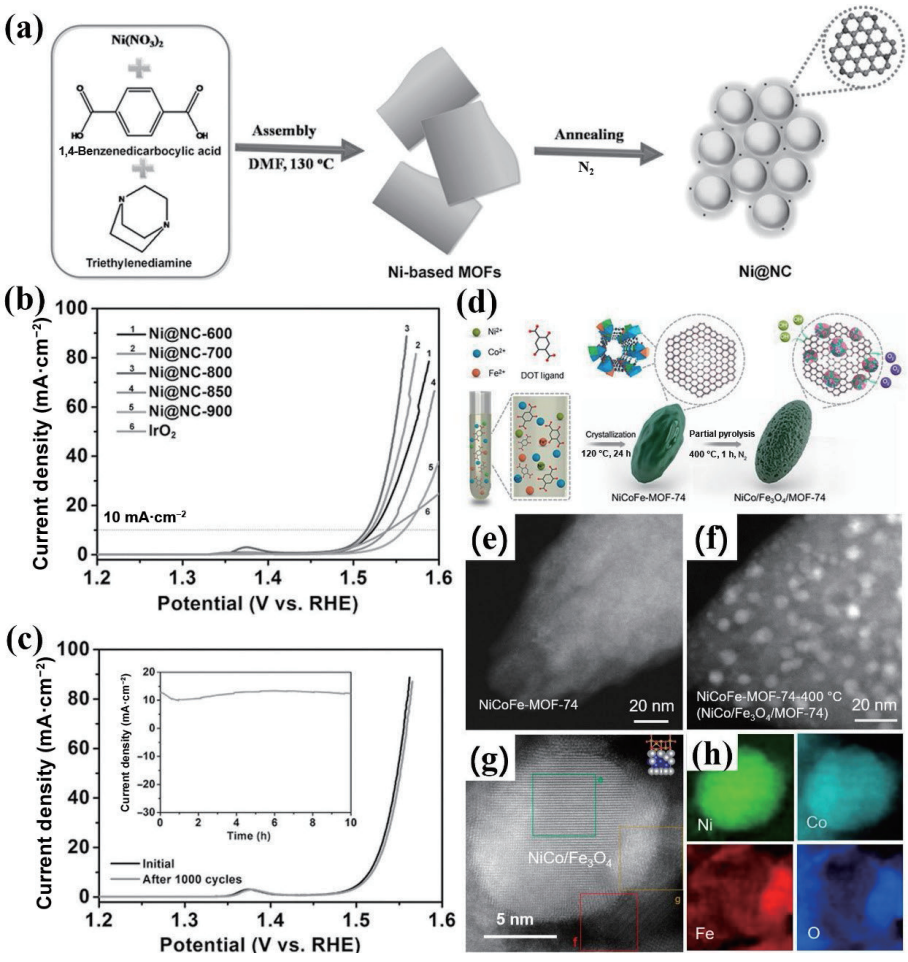

Figure 10 (a) Schematic illustration of the preparation of 2D Ni-MOF-derived Ni@NC. (b) and (c) The OER LSV curves of Ni@NC at different temperatures and IrO_2. (c) Stability test chart of Ni@NC-800. Reproduced with permission from Ref. [148], © WILEY-VCH Verlag GmbH & Co. KGaA, Weinheim 2017. (d) Schematic diagram of the preparation scheme of trimetallic NiCoFe-MOF-74 and its derivatives. (e) SEM image of NiCoFe-MOF-74. (f) SEM image of NiCoFe-MOF-74-derived materials. (g) HRTEM image of NiCoFe-MOF-74-derived materials and (h) corresponding STEM-EELS elemental mappings. Reproduced with permission from Ref. [156], © American Chemical Society 2018.

overpotential of 560 mV, which shows better performance than RuO_2 (the maximum current density of RuO_2 can only reach about 44 mA·cm^{-2}). Dong and coworkers reported the encapsulation of highly dispersed Co nanoparticles on N-doped 2D carbon skeleton composited carbon nanotubes (Co-NCS@CNTs) by pyrolyzing 2D ZIF (ZIF-L) nanosheets at high temperature under H_2-Ar gas mixture [169]. SEM and TEM confirmed that the pyrolysis product maintained the basic skeleton of the precursor nanosheet (the thickness was only 30 nm), and the Co catalyst particles were wrapped at the tip of the carbon nanotube with a diameter of 10 nm, avoiding the metal agglomeration at high-temperature. Based on the advantages of structure, Co-NCS@CNT exhibited lower overpotential than pure MOF products (Co-NCP and Co-NCS) at 10 mA·cm^{-2} current density. The lower Tafel slope (92.9 mV·dec^{-1}) than Ir/C also proved the fast reaction kinetic rate of Co-NCS@CNT. Compared with single metal/carbon, alloys/carbon tends to exhibit better OER catalytic activity because metal-to-metal interactions regulate the electronic structure and microstructure of materials. Taking Fe_1Co_3/V_O-800 synthesized by Zhang et al. as an example, it was carbonized from Fe-doped Co-based 2D MOF nanosheets [170]. The introduction of Fe could effectively adjust the electronic structure and enhance the catalytic activity of the catalysts. The mesoporous and interconnect morphology of triangular nanosheets leads to shorter electron transport paths and higher transfer rates. The synergistic effect of Fe and Co atomic centers significantly improved the OER performance. Specifically, Fe_1Co_3/V_O-800 only required a low overpotential of 260 mV and a small Tafel slope of 53 mV·dec^{-1} to achieve a current density of 10 mA·cm^{-2} in 1.0 M KOH. Metal/alloys catalysts formed from MOF pyrolysis have shown good OER catalytic performance, but the synthesis conditions such as higher temperatures, special atmosphere, or precursors need to be considered. The oxides formed by pyrolysis at 200 to 600 °C are encapsulated in the framework, which can make full use of the structural characteristics of MOF to better expose the active sites. ZIF-67 nanosheets were annealed at 400 °C in air atmosphere, and An et al. obtained M-Co_3O_4 [172]. The characterization results confirmed the porous morphology of the annealed products, which was basically the same as that of the precursors. The 2D ultra-thin and closely connected morphology between nanosheets promoted mass and charge transfer, and the highly exposed Co sites and oxygen vacancies improved the catalytic efficiency. Thus M-Co_3O_4 showed excellent OER catalytic performance. Li et al. constructed metal oxide/carbon (such as Co_3O_4/C, NiO/C, and Cu_2O/C) using layered 2D MOFs as templates [24]. The experimental results showed that the method could inhibit the aggregation of oxide particles, thus madding the oxide particles evenly distributed in carbon, improving the conductivity, providing an effective way for rapid electron transfer, and ensuring the high durability in the OER process. The high specific surface area and abundant hierarchical pore structure of the synthesized products promoted the exposure of oxide active sites and further enhanced the catalytic activity of OER. 2D MOF

derived polymetallic oxides can exhibit better OER catalytic performance than single metal oxide based electrocatalysts due to their unique heterostructure and optimized electronic structure. Yang et al. synthesized ultra-thin zinc cobalt oxide nanosheets doped in nitrogen and carbon ($ZnCo_2O_4$@NCNWAs), which was formed from 2D Co-MOF by ion exchange and annealing [95]. The reasonable doping of Zn^{2+} optimized the structure and reduced the intrinsic band gap, resulting in improving the ion transmission efficiency and electronic conductivity. At the current density of 10 mA·cm^{-2}, $ZnCo_2O_4$@NC/CTs required an overpotential of only 379.6 mV, which was 175.6 mV less than Co_3O_4@NC/CT. Annealing at a relatively low temperature may generate metal/oxide heterostructures, which is also an important reason for the improvement of OER performance. Li et al. successfully synthesized NiCo/Fe_3O_4/MOF-74 by pyrolyzing NiCoFe-MOF nanosheets at 400 °C (Fig. 10(d)) [156]. As shown in Figs. 10(e) and 10(f), the MOF surface becomes rough after pyrolysis. Thermogravimetric analysis showed that Ni and Co were first decomposed and enriched in the nucleus, while Fe was deposited on the surface of the nanoparticles as a surface layer, and finally formed the NiCo/Fe_3O_4 active center. Furthermore, the perfect match of the distribution of O and that of Fe also indicated that the nanoparticles had metal NiCo alloys and Fe oxides (Figs. 10(g) and 10(h)). Experiments and theoretical calculations confirmed the excellent OER catalytic activity of NiCo/Fe_3O_4 active center. The Tafel slope was only 29 mV·dec^{-1}, and the calculated overpotential was only 250 mV. Yang et al. also obtained $FeNi_3$-Fe_3O_4 by pyrolyzing NiFe-MOF nanosheets [98], and the pyrolysis products have an overpotential of 234 mV at a current density of 10 mA·cm^{-2}. The metal/alloy/oxide with 2D structure produced by MOF pyrolysis have been widely investigated as OER electrocatalysts due to highly exposed active sites, large specific surface area, and easily conductive carbon skeleton. However, because of the lack of research on the formation process of active center particles (for example, the size of metal clusters and the formation of oxygen vacancies), further research is urgently needed to explore the relationship between the formation process and catalytic properties.

4.2.3 *Metal sulfides/selenides/phosphides*

Due to the similar characteristics with 2D MOF-derived metal oxides, 2D MOF-derived metal sulfides have been explored as electrocatalysts for oxygen evolution [25, 94, 147, 150, 158, 173, 174]. Besides, adjustable metal-sulfur coordination environment and good conductivity can also help metal sulfides obtain high OER catalytic activity. For example, Li et al. *in situ* grown 2D Ni-BDC on nickel substrate, and then liquid-phase vulcanized partially to synthesize Ni-BDC@NiS with hierarchically structure [173]. In a series of Ni-BDC@NiS vulcanized at different durations, Ni-BDC@NiS soaked for 12 h exhibited the best OER catalytic activity. At the current density of 20 mA·cm^{-2}, the optimal electrocatalyst exhibited a much lower overpotential of 330 mV than IrO_2/C (400 mV), NiS (420 mV), Ni-BDC (450 mV), and $Ni(OH)_2$ (460 mV). The results confirmed that partial vulcanization can not only maintain the rich active sites given by porous MOF, but also improve the rapid charge transfer rate and water-absorption capacity. Considering the regulating effect of Fe, Hu et al. also synthesized NiFe MS/MOF@NF nanosheets [158]. The Raman spectra proved that the Ni/Fe oxyhydroxides converted by MOFs in OER process are the true active site, which can strengthen the adsorption of oxygenated intermediates. Furthermore, metal sulfide clusters donate electrons from electron-rich metal atoms to Ni and Fe centers on the surface, which can accelerate OER kinetics. For the above reasons, the overpotential only required 230 mV at the current density of 50 mA·cm^{-2}. Compared with liquid-phase vulcanization, solid vulcanization is more flexible, and the carbon skeleton provided by MOF can further improve the conductivity and structural stability in the OER process. Zang et al. synthesized heteroatom-doped Co_9S_8@TDC by simply carbonizing Co-MOF precursors [174]. Because of the inherent activity of Co_9S_8 nanoparticles and the carbon shell doped with heteroatoms, Co_9S_8@TDC had excellent electrocatalytic activity for OER, which exhibited a lower overpotential of 330 mV at a current density of 10 mA·cm^{-2}. Liu et al. used pyridine as a 2D morphology inhibitor to obtain Ni based MOF nanosheets precursor via a simple solvothermal method, and then pyrolyzed to synthesize Ni-Ni_3S_2@Carbon at high temperature [147]. The existence of SO_4^{2-} leaded to the pyrolysis process without introducing additional sulfur sources. MOF carbon skeleton limited the aggregation of Ni_3S_2 nanoparticles at high temperature and the carbon coated structure improved the stability and conductivity. At the same time, the N atoms in the organic ligands after pyrolysis were also involved in the regulation of the charge structure. Benefiting from the 2D morphology and component synergy of highly active Ni_3S_2 and N-doped carbon shells, the catalyst showed excellent OER performance. At alkaline conditions, only 284.7 mV overpotential was required to reach a current density of 10 mA·cm^{-2}. Zhang et al. reported a 2D metal sulfide derived from Co-based MOF (Fig. 11(a)) [150]. It can be clearly seen from the SEM images (Figs. 11(b) and 11(c)) that the nanosheets grow vertically on the carbon cloth. The 2D porous structure not only facilitated mass exchange and electron transfer in the electrocatalytic process, but also can accelerate reaction kinetics and enhance electrochemical reactions. As shown in Figs. 11(d) and 11(e), the introduction of nickel greatly improved the OER catalytic performance of Ni-Co-S with the overpotential of 270 mV at 10 mA·cm^{-2} in 1.0 M KOH solution and Tafel slope of 80 mV·dec^{-1}. Furthermore, the polarization curve change after 5000 CV cycles was negligible. As the elements of the same main family, selenium has strong non-metallic properties, which can not only ensure its better stability, but also make its conductivity significantly higher than that of sulfur. In addition, the electronegativity of selenium makes it more prone to undergo reversible electron gain/loss reactions, resulting in intermediate ions with higher electrochemical activity. The high conductivity and appropriate electronegativity of selenium help to reduce the overpotential of electrochemical reaction. Therefore, the selenides derived from 2D MOF have the strong potential to catalyze OER with high efficiency. For instance, using Co-MOF as a precursor, He and co-workers synthesized 2D CoSe/$MoSe_2$ by high-temperature selenization [99]. CoSe/$MoSe_2$ exhibited excellent OER performance with low overpotential (262 mV at 10 mA·cm^{-2}) and long-term stability (above 20 h). In addition, Sun et al. reported a MOF complex selenide, named NiFe-MOF/$NiSe_x$/NF, which showed excellent electrocatalytic OER activity with low overpotentials of 198 and 230 mV at the current densities of 10 and 100 mA·cm^{-2}, respectively, and long-term stability over 40 h [160]. The experimental results showed that the layered nanosheets structure exposed more active sites and promoted gas release, and the interlayer of $NiSe_x$ greatly improved the conductivity of the electrode.

Metal phosphides are frequently reported catalysts for OER due to their excellent conductivity and quasi metallic properties [93, 96, 146, 175, 176]. But unlike sulfides or selenides, phosphides often appear in the form of nanoparticles, which are easy to agglomerate during the synthesis process and lose the catalytic activity. 2D MOF derived carbon layer is expected to limit the agglomeration of metal phosphide nanoparticles and expose more active sites. Therefore, 2D MOF derived metal phosphides show remarkable OER electrocatalytic properties. Taking an example of

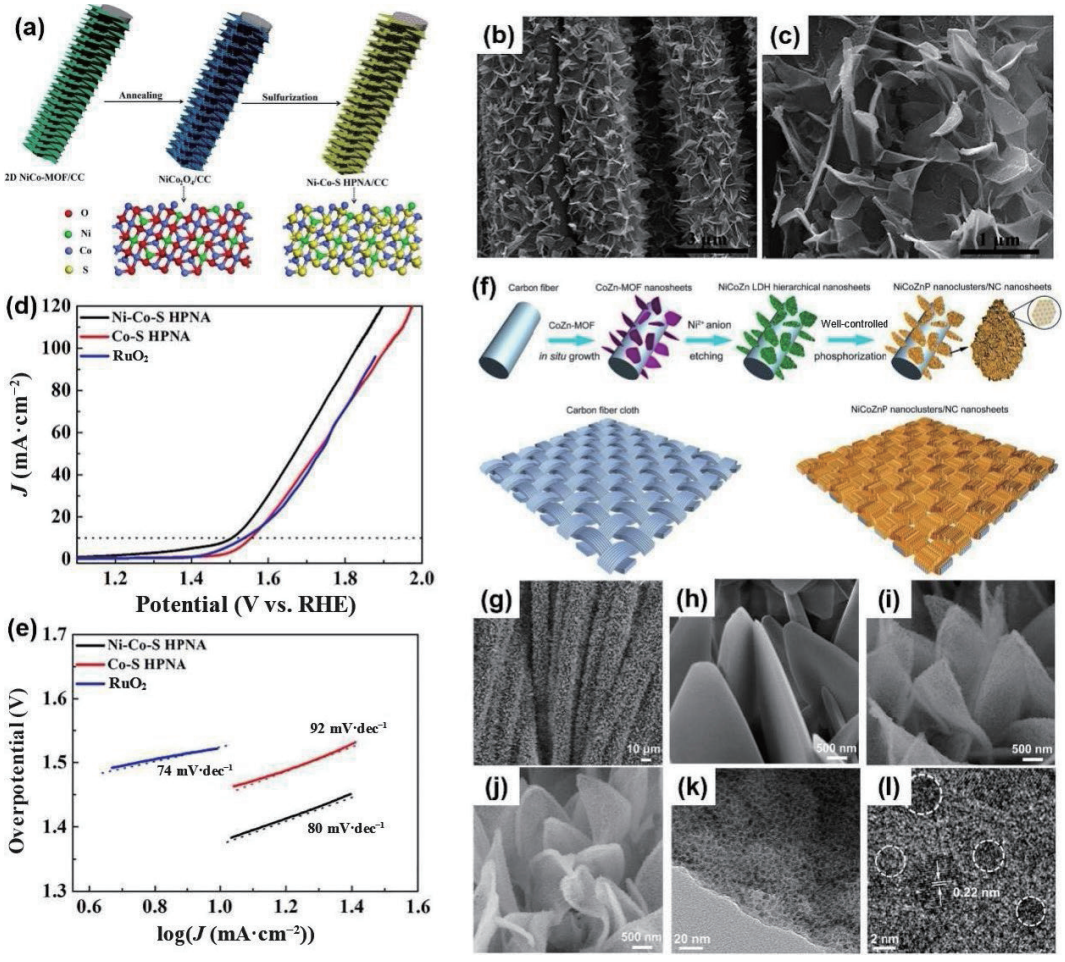

Figure 11 (a) Schematic diagram of preparation of Ni-Co-S HPNA/CC nanomaterials. (b) and (c) SEM images of Ni-Co-S HPNA/CC. (d) LSV curves. (e) Tafel plots. Reproduced with permission from Ref. [150], © Elsevier Inc. 2019. (f) Schematic diagram of preparation of NiCoZnP/NC nanosheet. (g) and (h) SEM images of CoZn-MOF nanoflakes. (i) SEM image of NiCoZn LDH nanosheets. (j) SEM image of NiCoZnP/NC nanosheet. (k) and (l) TEM images of NiCoZnP/NC nanosheet. Reproduced with permission from Ref. [159], © Elsevier B.V. 2021.

NiCoZnP prepared by Yong et al. (Fig. 11(f)), the SEM images (Figs. 11(g)–11(j)) indicated the MOF nanosheet has a smooth surface, but the material surface becomes rough after converting to NiCoZn LDH. After phosphating, the material surface remains rough. TEM images (Figs. 11(k) and 11(l)) showed that the size of NiCoZnP nanoclusters was only 3 nm and uniformly monodispersed on the hierarchical ultra-thin NC nanosheets after phosphating [159]. Ultrathin NC nanosheets and monodisperse ultra-fine NiCoZnP nanoclusters provide a large active area (959.1 mF·cm^{-2}) for OER, and the high conductivity brought by phosphating also reduces the contact resistance of the material (only 5.5 Ω), thus facilitating electron transport.

4.2.4 2D MOF-derived combined materials

2D MOF has the potential to become an excellent carrier owing to the large surface areas, abundant active exposure sites, preferable mass and charge transfer properties, and adjustable composition [81, 122]. Until now, many researchers have successfully loaded precious metals on 2D MOFs and achieved high catalytic activity as well as low loading. Taking an example of Ni-MOF nanosheets, Wang et al. designed a kind of composite nanomaterials based on Pt NPs embedded in 2D Ni-MOF, which exhibited superior OER catalytic activity (over RuO_2) even at extremely low loading (0.7 wt.%) [177]. XPS results and DFT calculation results exhibit that the electrons could be partially transferred from the metal nodes of 2D Ni-MOFs to the Pt NPs and the enhancement of OER activity originated from the synergistic effect between Pt NPs and 2D Ni-MOFs. Zhang et al. synthesized a series of catalysts that noble metal (M = Ir, Ru and Pt) evenly dispersed on 2D Ni-MOFs under mild synthesis conditions (fast mixing at ambient temperature) [151]. XPS results showed that many M–O–Ni bridging bonds spontaneously formed on the surface of 2D MOF nanosheets, leading to the anchoring of noble metal nanocrystals on 2D MOF nanosheets. In addition, the presence of M–O bonds and the red shift in the Ni 2p spectrum of M–O–Ni indicated that charge migrated from noble metal to Ni ions through oxygen-containing functional groups. Theoretical calculations also confirmed that the Ir–O–Ni bridging bonds ameliorated the electronic structures of both Ni sites and Ir sites, achieving the optimization of intermediate adsorption energy. In general, the large specific surface area of 2D MOFs and abundant unsaturated sites on the surface provide enough sites for the anchoring of precious metals. And the charge transfer between noble metals and 2D MOF nanosheets is also conducive to reducing the energy barrier of OER process.

5 Summary and outlook

Efficient electrocatalyst for OER is the core for reducing the cost of green hydrogen production and promoting the development of clean energy technology. This article has reviewed the preparation, characterization of 2D MOFs and derivatives, and the research progress as catalytic materials for OER. First, OER mechanism and several basic parameters for evaluating OER catalysts are briefly introduced, and then the representative synthesis methods for obtaining MOFs nanosheets and derivatives are discussed.

Finally, this review focuses on the latest progress in the design, synthesis, and the relationship between microstructure and composition and catalytic performance of 2D MOFs and their derivatives for OER. Fundamentally, the high OER activity of 2D MOF-based catalysts is mainly attributed to the following characteristics: (1) The large specific surface area and uniformly distributed metal sites provide lots of accessible active sites for OER. (2) The sheet structure promotes efficient mass transfer and electron transport. (3) The adjustable components and controllable topology are conducive to optimizing the electronic structure, reducing the reaction adsorption energy, and improving the activity of the catalyst. In addition, heteroatoms provided by specific organic ligands can promote the redistribution of electrons in materials, and increase redox active sites. Furthermore, the derivatives obtained from 2D MOF have stronger catalytic performance. On the one hand, the derivatives can retain the basic morphology of 2D MOF and have porous nanostructures. On the other hand, these derivatives have stronger conductivity and stability than 2D MOFs.

The strategy of using 2D MOFs as precursors has been shown to produce new materials with high electrocatalytic activity, which is expected to produce electrocatalysts with better performance in the future. Nevertheless, there are still several problems to be solved when 2D MOFs are used as OER catalytic material: (1) Expensive organic ligands and low yield synthesis methods increase the cost of MOF, limiting the large-scale synthesis of 2D MOFs. (2) Although many 2D MOFs have been reported to have excellent stability, the stability with industrial prospects (such as thousands of hours or longer) has not really appeared due to the instability of coordination bonds in MOFs. The stability of 2D MOFs and their derivatives under extreme conditions is also an issue that should be more concerned in the future. (3) Because the actual active species and catalytic sites are difficult to identify and characterize, the specific OER mechanism of 2D MOFs and their derivatives remains ambiguous. (4) At present, the preparation of MOF derivatives mostly adopts the pyrolysis method with high energy consumption, and the method with low energy consumption and high efficiency must be found.

In view of the above problems, some personal views are put forward on the future development of 2D MOFs and their derivatives in the field of OER electrocatalysis:

(1) The expensive cost of MOF reduces the margin for error in experiments. To achieve large-scale screening of 2D MOF and derivatives, it is wonderful way that developing new synthesis methods to improve the yield of 2D MOF and selecting cheaper 2D MOF to prepare derivatives, or replacing the traditional trial and error process through machine learning. High throughput theoretical calculation is an effective method to replace experimental synthesis, for example, designing reasonable doping, vacancy, heterostructure, or other models to adjust and optimize the electronic structure of materials and reduce the adsorption free energy of reaction intermediates on active sites, thus improving the overall catalytic performance of materials.

(2) The stability of 2D MOF is a controversial issue, especially in the complex catalytic environment. The degradation of MOFs usually involves two steps, namely, metal–ligand bond breaking and the formation of more stable products than the original MOFs [178]. Therefore, the chemical stability of MOFs depends to a large extent on the internal structure of MOFs, including the charge density and coordination number of metal nodes, pH, configuration, etc. The preparation of stable MOFs requires reasonable control of these key factors. In addition, 2D MOF is very unstable due to its high surface energy, which leads to agglomeration. This can be solved by adding stabilizer or using surfactant with similar surface energy as 2D MOF.

(3) The rapidly developing cutting-edge characterization technologies (such as XAFS, high-angle annular dark field STEM (HAADF-STEM), *in situ* FTIR spectroscopy, and Raman spectroscopy) can effectively observe various intermediates of OER reaction, which is crucial to the systematic study of the structure–activity relationship and catalytic mechanism in the OER process. In addition, theoretical calculation is also helpful to understand the electron transfer process in MOF catalyst of OER process and provide reliable evidence for studying the specific catalytic mechanism of OER [179].

(4) The purpose of preparing MOF derivatives is to enhance the stability and conductivity of MOF materials and improve their catalytic performance. In addition to completely transforming MOF into other substances, MOF nanosheets can also be combined with metal particles/clusters, metal oxides, and metal sulfides, or mixed with other 2D materials, and 2D MOF can be modified by defect engineering.

Acknowledgements

This work was supported by the National Natural Science Foundation of China (No. 21771191), Shandong Natural Science Fund (No. ZR2020KB010), and the Fundamental Research Funds for the Central Universities (No. 22CX07010A).

References

[1] Yu, J.; Li, B. Q.; Zhao, C. X.; Zhang, Q. Seawater electrolyte-based metal-air batteries: From strategies to applications. *Energy Environ. Sci.* **2020**, *13*, 3253–3268.

[2] Zhao, S. L.; Wang, Y.; Dong, J. C.; He, C. T.; Yin, H. J.; An, P. F.; Zhao, K.; Zhang, X. F.; Gao, C.; Zhang, L. J. et al. Ultrathin metal-organic framework nanosheets for electrocatalytic oxygen evolution. *Nat. Energy* **2016**, *1*, 16184.

[3] Lu, X. F.; Chen, Y.; Wang, S. B.; Gao, S. Y.; Lou, X. W. Interfacing manganese oxide and cobalt in porous graphitic carbon polyhedrons boosts oxygen electrocatalysis for Zn-air batteries. *Adv. Mater.* **2019**, *31*, 1902339.

[4] Huang, Z. F.; Song, J. J.; Du, Y. H.; Xi, S. B.; Dou, S.; Nsanzimana, J. M. V.; Wang, C.; Xu, Z. J.; Wang, X. Chemical and structural origin of lattice oxygen oxidation in Co-Zn oxyhydroxide oxygen evolution electrocatalysts. *Nat. Energy* **2019**, *4*, 329–338.

[5] Li, P. S.; Wang, M. Y.; Duan, X. X.; Zheng, L. R.; Cheng, X. P.; Zhang, Y. F.; Kuang, Y.; Li, Y. P.; Ma, Q.; Feng, Z. X. et al. Boosting oxygen evolution of single-atomic ruthenium through electronic coupling with cobalt-iron layered double hydroxides. *Nat. Commun.* **2019**, *10*, 1711.

[6] Zhang, K. X.; Zou, R. Q. Advanced transition metal-based OER electrocatalysts: Current status, opportunities, and challenges. *Small* **2021**, *17*, 2100129.

[7] Weng, B.; Xu, F.; Wang, C.; Meng, W.; Grice, C. R.; Yan, Y. A layered $Na_{1-x}Ni_yFe_{1-y}O_2$ double oxide oxygen evolution reaction electrocatalyst for highly efficient water-splitting. *Energy Environ. Sci.* **2017**, *10*, 121–128.

[8] Hu, Q.; Gao, K. R.; Wang, X. D.; Zheng, H. J.; Cao, J. Y.; Mi, L. R.; Huo, Q. H.; Yang, H. P.; Liu, J. H.; He, C. X. Subnanometric Ru clusters with upshifted D band center improve performance for alkaline hydrogen evolution reaction. *Nat. Commun.* **2022**, *13*, 3958.

[9] Shan, J. Q.; Zheng, Y.; Shi, B. Y.; Davey, K.; Qiao, S. Z. Regulating electrocatalysts via surface and interface engineering for acidic water electrooxidation. *ACS Energy Lett.* **2019**, *4*, 2719–2730.

[10] Seoane, B.; Coronas, J.; Gascon, I.; Benavides, M. E.; Karvan, O.; Caro, J.; Kapteijn, F.; Gascon, J. Metal-organic framework based mixed matrix membranes: A solution for highly efficient CO_2 capture. *Chem. Soc. Rev.* **2015**, *44*, 2421–2454.

[11] Zhang, H.; Xiao, Q.; Guo, X. H.; Li, N. J.; Kumar, P.; Rangnekar, N.; Jeon, M. Y.; Al-Thabaiti, S.; Narasimharao, K.; Basahel, S. N. et al. Open-pore two-dimensional MFI zeolite nanosheets for the fabrication of hydrocarbon-isomer-selective membranes on porous polymer supports. *Angew. Chem., Int. Ed.* **2016**, *55*, 7184–7187.

[12] Wang, J.; Hu, C.; Wang, Y. S.; Cui, H. Chemiluminescent two-dimensional metal-organic framework with multiple metal catalytic centers and its peroxidase-like activity for sensing of small molecules. *ACS Appl. Mater. Interfaces* **2022**, *14*, 3156–3164.

[13] Zhao, Y. W.; Guo, L. E.; Zhang, F. Q.; Yao, J.; Zhang, X. M. Turn-on fluorescence enantioselective sensing of hydroxyl carboxylic enantiomers by metal-organic framework nanosheets with a homochiral tetracarboxylate of cyclohexane diamide. *ACS Appl. Mater. Interfaces* **2021**, *13*, 20821–20829.

[14] He, C. B.; Liu, D. M.; Lin, W. B. Nanomedicine applications of hybrid nanomaterials built from metal-ligand coordination bonds: Nanoscale metal-organic frameworks and nanoscale coordination polymers. *Chem. Rev.* **2015**, *115*, 11079–11108.

[15] Qin, Y. T.; Li, Z. X.; Duan, Y. L.; Guo, J.; Zhao, M. T.; Tang, Z. Y. Nanostructural engineering of metal-organic frameworks: Construction strategies and catalytic applications. *Matter* **2022**, *5*, 3260–3310.

[16] Jiang, Q. Y.; Zhou, C. H.; Meng, H. B.; Han, Y.; Shi, X. F.; Zhan, C. H.; Zhang, R. F. Two-dimensional metal-organic framework nanosheets: Synthetic methodologies and electrocatalytic applications. *J. Mater. Chem. A* **2020**, *8*, 15271–15301.

[17] Lei, J.; Zeng, M. Q.; Fu, L. Two-dimensional metal-organic frameworks as electrocatalysts for oxygen evolution reaction. *Chem. Res. Chin. Univ.* **2020**, *36*, 504–510.

[18] Hu, Q.; Qin, Y. J.; Wang, X. D.; Wang, Z. Y.; Huang, X. W.; Zheng, H. J.; Gao, K. R.; Yang, H. P.; Zhang, P. X.; Shao, M. H. et al. Reaction intermediate-mediated electrocatalyst synthesis favors specified facet and defect exposure for efficient nitrate-ammonia conversion. *Energy Environ. Sci.* **2021**, *14*, 4989–4997.

[19] Chang, C.; Chen, W.; Chen, Y.; Chen, Y. H.; Chen, Y.; Ding, F.; Fan, C. H.; Fan, H. J.; Fan, Z. X.; Gong, C. et al. Recent progress on two-dimensional materials. *Acta Phys. Chim. Sin.* **2021**, *37*, 2108017.

[20] Peng, Y.; Li, Y. S.; Ban, Y. J.; Yang, W. S. Two-dimensional metal-organic framework nanosheets for membrane-based gas separation. *Angew. Chem., Int. Ed.* **2017**, *56*, 9757–9761.

[21] Kim, J.; Lee, S.; Kim, J.; Lee, D. Metal-organic frameworks derived from zero-valent metal substrates: Mechanisms of formation and modulation of properties. *Adv. Funct. Mater.* **2019**, *29*, 1808466.

[22] Huo, J. M.; Wang, Y.; Meng, J.; Zhao, X. Y.; Zhai, Q. G.; Jiang, Y. C.; Hu, M. C.; Li, S. N.; Chen, Y. π···π interaction directed 2D FeNi-LDH nanosheets from 2D Hofmann-MOFs for the oxygen evolution reaction. *J. Mater. Chem. A* **2022**, *10*, 1815–1820.

[23] Li, Y. W.; Lu, M. T.; He, P. P.; Wu, Y. H.; Wang, J. W.; Chen, D. N.; Xu, H.; Gao, J. K.; Yao, J. M. Bimetallic metal-organic framework-derived nanosheet-assembled nanoflower electrocatalysts for efficient oxygen evolution reaction. *Chem. Asian J.* **2019**, *14*, 1590–1594.

[24] Zhou, J.; Dou, Y. B.; Zhou, A. W.; Shu, L.; Chen, Y.; Li, J. R. Layered metal-organic framework-derived metal oxide/carbon nanosheet arrays for catalyzing the oxygen evolution reaction. *ACS Energy Lett.* **2018**, *3*, 1655–1661.

[25] Yuan, B. B.; Li, C. Q.; Guan, L. H.; Li, K.; Lin, Y. Q. Prussian blue analog nanocubes tuning synthesis of coral-like Ni_3S_2@Mil-53(NiFeCo) core–shell nanowires array and boosting oxygen evolution reaction. *J. Power Sources* **2020**, *451*, 227295.

[26] Hou, C. C.; Zou, L. L.; Wang, Y.; Xu, Q. MOF-mediated fabrication of a porous 3D superstructure of carbon nanosheets decorated with ultrafine cobalt phosphide nanoparticles for efficient electrocatalysis and zinc-air batteries. *Angew. Chem., Int. Ed.* **2020**, *59*, 21360–21366.

[27] Sahu, N.; Das, J. K.; Behera, J. N. Metal-organic framework (MOF) derived flower-shaped $CoSe_2$ nanoplates as a superior bifunctional electrocatalyst for both oxygen and hydrogen evolution reactions. *Sustainable Energy Fuels* **2021**, *5*, 4992–5000.

[28] Wang, X. P.; Xi, S. B.; Huang, P. R.; Du, Y. H.; Zhong, H. Y.; Wang, Q.; Borgna, A.; Zhang, Y. W.; Wang, Z. B.; Wang, H. et al. Pivotal role of reversible NiO_6 geometric conversion in oxygen evolution. *Nature* **2022**, *611*, 702–708.

[29] Hong, W. T.; Risch, M.; Stoerzinger, K. A.; Grimaud, A.; Suntivich, J.; Shao-Horn, Y. Toward the rational design of non-precious transition metal oxides for oxygen electrocatalysis. *Energy Environ. Sci.* **2015**, *8*, 1404–1427.

[30] Damjanovic, A.; Jovanovic, B. Anodic oxide films as barriers to charge transfer in O_2 evolution at Pt in acid solutions. *J. Electrochem. Soc.* **1976**, *123*, 374–381.

[31] Binninger, T.; Mohamed, R.; Waltar, K.; Fabbri, E.; Levecque, P.; Kötz, R.; Schmidt, T. J. Thermodynamic explanation of the universal correlation between oxygen evolution activity and corrosion of oxide catalysts. *Sci. Rep.* **2015**, *5*, 12167.

[32] Hardin, W. G.; Slanac, D. A.; Wang, X. Q.; Dai, S.; Johnston, K. P.; Stevenson, K. J. Highly active, nonprecious metal perovskite electrocatalysts for bifunctional metal-air battery electrodes. *J. Phys. Chem. Lett.* **2013**, *4*, 1254–1259.

[33] Hardin, W. G.; Mefford, J. T.; Slanac, D. A.; Patel, B. B.; Wang, X. Q.; Dai, S.; Zhao, X.; Ruoff, R. S.; Johnston, K. P.; Stevenson, K. J. Tuning the electrocatalytic activity of perovskites through active site variation and support interactions. *Chem. Mater.* **2014**, *26*, 3368–3376.

[34] Grimaud, A.; Diaz-Morales, O.; Han, B. H.; Hong, W. T.; Lee, Y. L.; Giordano, L.; Stoerzinger, K. A.; Koper, M. T. M.; Shao-Horn, Y. Activating lattice oxygen redox reactions in metal oxides to catalyse oxygen evolution. *Nat. Chem.* **2017**, *9*, 457–465.

[35] Forslund, R. P.; Hardin, W. G.; Rong, X.; Abakumov, A. M.; Filimonov, D.; Alexander, C. T.; Mefford, J. T.; Iyer, H.; Kolpak, A. M.; Johnston, K. P. et al. Exceptional electrocatalytic oxygen evolution via tunable charge transfer interactions in $La_{0.5}Sr_{1.5}Ni_{1-x}Fe_xO_{4\pm\delta}$ ruddlesden-popper oxides. *Nat. Commun.* **2018**, *9*, 3150.

[36] Li, X.; Wang, H.; Cui, Z. M.; Li, Y. T.; Xin, S.; Zhou, J. S.; Long, Y. W.; Jin, C. Q.; Goodenough, J. B. Exceptional oxygen evolution reactivities on $CaCoO_3$ and $SrCoO_3$. *Sci. Adv.* **2019**, *5*, eaav6262.

[37] Pan, Y. L.; Xu, X. M.; Zhong, Y. J.; Ge, L.; Chen, Y. B.; Veder, J. P. M.; Guan, D. Q.; O'Hayre, R.; Li, M. R.; Wang, G. X. et al. Direct evidence of boosted oxygen evolution over perovskite by enhanced lattice oxygen participation. *Nat. Commun.* **2020**, *11*, 2002.

[38] Zhang, N.; Feng, X. B.; Rao, D. W.; Deng, X.; Cai, L. J.; Qiu, B. C.; Long, R.; Xiong, Y. J.; Lu, Y.; Chai, Y. Lattice oxygen activation enabled by high-valence metal sites for enhanced water oxidation. *Nat. Commun.* **2020**, *11*, 4066.

[39] Lee, S.; Banjac, K.; Lingenfelder, M.; Hu, X. L. Oxygen isotope labeling experiments reveal different reaction sites for the oxygen evolution reaction on nickel and nickel iron oxides. *Angew. Chem., Int. Ed.* **2019**, *58*, 10295–10299.

[40] Roy, C.; Sebok, B.; Scott, S. B.; Fiordaliso, E. M.; Sørensen, J. E.; Bodin, A.; Trimarco, D. B.; Damsgaard, C. D.; Vesborg, P. C. K.; Hansen, O. et al. Impact of nanoparticle size and lattice oxygen on water oxidation on $NiFeO_xH_y$. *Nat. Catal.* **2018**, *1*, 820–829.

[41] Li, S. S.; Gao, Y. Q.; Li, N.; Ge, L.; Bu, X. H.; Feng, P. Y. Transition metal-based bimetallic MOFs and MOF-derived catalysts for electrochemical oxygen evolution reaction. *Energy Environ. Sci.* **2021**, *14*, 1897–1927.

[42] McCrory, C. C. L.; Jung, S.; Ferrer, I. M.; Chatman, S. M.; Peters, J. C.; Jaramillo, T. F. Benchmarking hydrogen evolving reaction and oxygen evolving reaction electrocatalysts for solar water splitting devices. *J. Am. Chem. Soc.* **2015**, *137*, 4347–4357.

[43] Suen, N. T.; Hung, S. F.; Quan, Q.; Zhang, N.; Xu, Y. J.; Chen, H. M. Electrocatalysis for the oxygen evolution reaction: Recent development and future perspectives. *Chem. Soc. Rev.* **2017**, *46*, 337–365.

[44] Li, M.; Gu, Y.; Chang, Y. J.; Gu, X. C.; Tian, J. Q.; Wu, X.; Feng, L. G. Iron doped cobalt fluoride derived from CoFe layered double hydroxide for efficient oxygen evolution reaction. *Chem. Eng. J.* **2021**, *425*, 130686.

[45] Li, G. L.; Zhang, X. B.; Zhang, H.; Liao, C. Y.; Jiang, G. B. Bottom-

up MOF-intermediated synthesis of 3D hierarchical flower-like cobalt-based homobimetallic phophide composed of ultrathin nanosheets for highly efficient oxygen evolution reaction. *Appl. Catal. B: Environ.* **2019**, *249*, 147–154.

[46] Zhao, K. M.; Zhu, W. W.; Liu, S. Q.; Wei, X. L.; Ye, G. Y.; Su, Y. K.; He, Z. Two-dimensional metal-organic frameworks and their derivatives for electrochemical energy storage and electrocatalysis. *Nanoscale Adv.* **2020**, *2*, 536–562.

[47] Xue, Y. P.; Zhao, G. C.; Yang, R. Y.; Chu, F.; Chen, J.; Wang, L.; Huang, X. B. 2D metal-organic framework-based materials for electrocatalytic, photocatalytic and thermocatalytic applications. *Nanoscale* **2021**, *13*, 3911–3936.

[48] Zhao, M. T.; Lu, Q. P.; Ma, Q. L.; Zhang, H. Two-dimensional metal-organic framework nanosheets. *Small Methods* **2017**, *1*, 1600030.

[49] Zhao, M. T.; Huang, Y.; Peng, Y. W.; Huang, Z. Q.; Ma, Q. L.; Zhang, H. Two-dimensional metal-organic framework nanosheets: Synthesis and applications. *Chem. Soc. Rev.* **2018**, *47*, 6267–6295.

[50] Duan, J. G.; Li, Y. S.; Pan, Y. C.; Behera, N.; Jin, W. Q. Metal-organic framework nanosheets: An emerging family of multifunctional 2D materials. *Coord. Chem. Rev.* **2019**, *395*, 25–45.

[51] Peng, Y.; Yang, W. S. 2D metal-organic framework materials for membrane-based separation. *Adv. Mater. Interfaces* **2020**, *7*, 1901514.

[52] Varsha, M. V.; Nageswaran, G. Review—2D layered metal organic framework nanosheets as an emerging platform for electrochemical sensing. *J. Electrochem. Soc.* **2020**, *167*, 136502.

[53] Zhu, A. X.; Dou, A. N.; Fang, X. D.; Yang, L. B.; Xu, Q. Q. Retracted article: Chemical etching of a cobalt-based metal-organic framework for enhancing the electrocatalytic oxygen evolution reaction. *J. Mater. Chem. A*, in press, https://doi.org/10.1039/C7TA02103H.

[54] Zhao, H. A.; Yu, L.; Zhang, L. T.; Dai, L. M.; Yao, F. L.; Huang, Y.; Sun, J. W.; Zhu, J. W. Facet engineering in ultrathin two-dimensional NiFe metal-organic frameworks by coordination modulation for enhanced electrocatalytic water oxidation. *ACS Sustainable Chem. Eng.* **2021**, *9*, 10892–10901.

[55] Amo-Ochoa, P.; Welte, L.; González-Prieto, R.; Sanz Miguel, P. J.; Gómez-García, C. J.; Mateo-Martí, E.; Delgado, S.; Gómez-Herrero, J.; Zamora, F. Single layers of a multifunctional laminar Cu(I, II) coordination polymer. *Chem. Commun.* **2010**, *46*, 3262–3264.

[56] Kondo, A.; Tiew, C. C.; Moriguchi, F.; Maeda, K. Fabrication of metal-organic framework nanosheets and nanorolls with N-donor type bridging ligands. *Dalton Trans.* **2013**, *42*, 15267–15270.

[57] Foster, J. A.; Henke, S.; Schneemann, A.; Fischer, R. A.; Cheetham, A. K. Liquid exfoliation of alkyl-ether functionalised layered metal-organic frameworks to nanosheets. *Chem. Commun.* **2016**, *52*, 10474–10477.

[58] Li, P. Z.; Maeda, Y.; Xu, Q. Top-down fabrication of crystalline metal-organic framework nanosheets. *Chem. Commun.* **2011**, *47*, 8436–8438.

[59] Saines, P. J.; Tan, J. C.; Yeung, H. H. M.; Barton, P. T.; Cheetham, A. K. Layered inorganic–organic frameworks based on the 2, 2-dimethylsuccinate ligand: Structural diversity and its effect on nanosheet exfoliation and magnetic properties. *Dalton Trans.* **2012**, *41*, 8585–8593.

[60] Luo, Y. H.; Chen, C.; He, C.; Zhu, Y. Y.; Hong, D. L.; He, X. T.; An, P. J.; Wu, H. S.; Sun, B. W. Single-layered two-dimensional metal-organic framework nanosheets as an *in situ* visual test paper for solvents. *ACS Appl. Mater. Interfaces* **2018**, *10*, 28860–28867.

[61] Beldon, P. J.; Tominaka, S.; Singh, P.; Saha Dasgupta, T.; Bithell, E. G.; Cheetham, A. K. Layered structures and nanosheets of pyrimidinethiolate coordination polymers. *Chem. Commun.* **2014**, *50*, 3955–3957.

[62] Xu, H.; Gao, J. K.; Qian, X. F.; Wang, J. P.; He, H. J.; Cui, Y. J.; Yang, Y.; Wang, Z. Y.; Qian, G. D. Metal-organic framework nanosheets for fast-response and highly sensitive luminescent sensing of Fe^{3+}. *J. Mater. Chem. A* **2016**, *4*, 10900–10905.

[63] Tan, J. C.; Saines, P. J.; Bithell, E. G.; Cheetham, A. K. Hybrid nanosheets of an inorganic–organic framework material: Facile synthesis, structure, and elastic properties. *ACS Nano* **2012**, *6*, 615–621.

[64] Gomez, G. E.; Bernini, M. C.; Brusau, E. V.; Narda, G. E.; Vega, D.; Kaczmarek, A. M.; Van Deun, R.; Nazzarro, M. Layered exfoliable crystalline materials based on Sm-, Eu- and Eu/Gd-2-phenylsuccinate frameworks. Crystal structure, topology and luminescence properties. *Dalton Trans.* **2015**, *44*, 3417–3429.

[65] Wang, H. S.; Li, J.; Li, J. Y.; Wang, K.; Ding, Y.; Xia, X. H. Lanthanide-based metal-organic framework nanosheets with unique fluorescence quenching properties for two-color intracellular adenosine imaging in living cells. *NPG Asia Mater.* **2017**, *9*, e354–e354.

[66] Cliffe, M. J.; Castillo-Martínez, E.; Wu, Y.; Lee, J.; Forse, A. C.; Firth, F. C. N.; Moghadam, P. Z.; Fairen-Jimenez, D.; Gaultois, M. W.; Hill, J. A. et al. Metal-organic nanosheets formed via defect-mediated transformation of a hafnium metal-organic framework. *J. Am. Chem. Soc.* **2017**, *139*, 5397–5404.

[67] Chandrasekhar, P.; Mukhopadhyay, A.; Savitha, G.; Moorthy, J. N. Orthogonal self-assembly of a trigonal triptycene triacid: Signaling of exfoliation of porous 2D metal-organic layers by fluorescence and selective CO_2 capture by the hydrogen-bonded MOF. *J. Mater. Chem. A* **2017**, *5*, 5402–5412.

[68] Hai, G. T.; Jia, X. L.; Zhang, K. Y.; Liu, X.; Wu, Z. Y.; Wang, G. High-performance oxygen evolution catalyst using two-dimensional ultrathin metal-organic frameworks nanosheets. *Nano Energy* **2018**, *44*, 345–352.

[69] Wei, X. F.; Wang, S.; Hua, Z. L.; Chen, L. S.; Shi, J. L. Metal-organic framework nanosheet electrocatalysts for efficient H_2 production from methanol solution: Methanol-assisted water splitting or methanol reforming. *ACS Appl. Mater. Interfaces* **2018**, *10*, 25422–25428.

[70] Pang, W.; Shao, B.; Tan, X. Q.; Tang, C.; Zhang, Z.; Huang, J. Exfoliation of metal-organic frameworks into efficient single-layer metal-organic nanosheet electrocatalysts by the synergistic action of host−guest interactions and sonication. *Nanoscale* **2020**, *12*, 3623–3629.

[71] Han, L. J.; Zheng, D.; Chen, S. G.; Zheng, H. G.; Ma, J. A highly solvent-stable metal-organic framework nanosheet: Morphology control, exfoliation, and luminescent property. *Small* **2018**, *14*, 1703873.

[72] Gallego, A.; Hermosa, C.; Castillo, O.; Berlanga, I.; Gómez-García, C. J.; Mateo-Martí, E.; Martínez, J. I.; Flores, F.; Gómez-Navarro, C.; Gómez-Herrero, J. et al. Solvent-induced delamination of a multifunctional two dimensional coordination polymer. *Adv. Mater.* **2013**, *25*, 2141–2146.

[73] Wang, X. R.; Chi, C. L.; Zhang, K.; Qian, Y. H.; Gupta, K. M.; Kang, Z. X.; Jiang, J. W.; Zhao, D. Reversed thermo-switchable molecular sieving membranes composed of two-dimensional metal-organic nanosheets for gas separation. *Nat. Commun.* **2017**, *8*, 14460.

[74] Peng, Y.; Li, Y. S.; Ban, Y. J.; Jin, H.; Jiao, W. M.; Liu, X. L.; Yang, W. S. Metal-organic framework nanosheets as building blocks for molecular sieving membranes. *Science* **2014**, *346*, 1356–1359.

[75] Ding, Y. J.; Chen, Y. P.; Zhang, X. L.; Chen, L.; Dong, Z. H.; Jiang, H. L.; Xu, H. X.; Zhou, H. C. Controlled intercalation and chemical exfoliation of layered metal-organic frameworks using a chemically labile intercalating agent. *J. Am. Chem. Soc.* **2017**, *139*, 9136–9139.

[76] Song, W. J. Intracellular DNA and microRNA sensing based on metal-organic framework nanosheets with enzyme-free signal amplification. *Talanta* **2017**, *170*, 74–80.

[77] Zhao, M. T.; Wang, Y. X.; Ma, Q. L.; Huang, Y.; Zhang, X.; Ping, J. F.; Zhang, Z. C.; Lu, Q. P.; Yu, Y. F.; Xu, H. et al. Ultrathin 2D metal-organic framework nanosheets. *Adv. Mater.* **2015**, *27*, 7372–7378.

[78] Choi, E. Y.; Barron, P. M.; Novotny, R. W.; Son, H. T.; Hu, C. H.; Choe, W. Pillared porphyrin homologous series: Intergrowth in metal-organic frameworks. *Inorg. Chem.* **2009**, *48*, 426–428.

[79] Gascon, J.; Aktay, U.; Hernandez-Alonso, M. D.; Van Klink, G. P.

M.; Kapteijn, F. Amino-based metal-organic frameworks as stable, highly active basic catalysts. *J. Catal.* **2009**, *261*, 75–87.

[80] Chen, J. Y.; Zhuang, P. Y.; Ge, Y. C.; Chu, H.; Yao, L. Y.; Cao, Y. D.; Wang, Z. Y.; Chee, M. O. L.; Dong, P.; Shen, J. F. et al. Sublimation-vapor phase pseudomorphic transformation of template-directed MOFs for efficient oxygen evolution reaction. *Adv. Funct. Mater.* **2019**, *29*, 1903875.

[81] Yang, L.; Zhu, G. L.; Wen, H.; Guan, X.; Sun, X.; Feng, H.; Tian, W. L.; Zheng, D. C.; Cheng, X. W.; Yao, Y. D. Constructing a highly oriented layered MOF nanoarray from a layered double hydroxide for efficient and long-lasting alkaline water oxidation electrocatalysis. *J. Mater. Chem. A* **2019**, *7*, 8771–8776.

[82] Sun, F. Z.; Wang, G.; Ding, Y. Q.; Wang, C.; Yuan, B. B.; Lin, Y. Q. NiFe-based metal-organic framework nanosheets directly supported on nickel foam acting as robust electrodes for electrochemical oxygen evolution reaction. *Adv. Energy Mater.* **2018**, *8*, 1800584.

[83] Huang, L.; Zhang, X.; Han, Y.; Wang, Q.; Fang, Y.; Dong, S. *In situ* synthesis of ultrathin metal-organic framework nanosheets: A new method for 2D metal-based nanoporous carbon electrocatalysts. *J. Mater. Chem. A* **2017**, *5*, 18610–18617.

[84] Hu, A. Q.; Pang, Q. Q.; Tang, C.; Bao, J. X.; Liu, H. Q.; Ba, K.; Xie, S. H.; Chen, J.; Chen, J. H.; Yue, Y. W. et al. Epitaxial growth and integration of insulating metal-organic frameworks in electrochemistry. *J. Am. Chem. Soc.* **2019**, *141*, 11322–11327.

[85] Huang, X.; Sheng, P.; Tu, Z. Y.; Zhang, F. J.; Wang, J. H.; Geng, H.; Zou, Y.; Di, C. A.; Yi, Y. P.; Sun, Y. M. et al. A two-dimensional π-d conjugated coordination polymer with extremely high electrical conductivity and ambipolar transport behaviour. *Nat. Commun.* **2015**, *6*, 7408.

[86] Dong, R. H.; Pfeffermann, M.; Liang, H. W.; Zheng, Z. K.; Zhu, X.; Zhang, J.; Feng, X. L. Large-area, free-standing, two-dimensional supramolecular polymer single-layer sheets for highly efficient electrocatalytic hydrogen evolution. *Angew. Chem., Int. Ed.* **2015**, *54*, 12058–12063.

[87] Lahiri, N.; Lotfizadeh, N.; Tsuchikawa, R.; Deshpande, V. V.; Louie, J. Hexaaminobenzene as a building block for a family of 2D coordination polymers. *J. Am. Chem. Soc.* **2017**, *139*, 19–22.

[88] Huang, J. K.; Li, M. L.; Wan, Y.; Dey, S.; Ostwal, M.; Zhang, D. L.; Yang, C. W.; Su, C. J.; Jeng, U. S.; Ming, J. et al. Functional two-dimensional coordination polymeric layer as a charge barrier in Li-S batteries. *ACS Nano* **2018**, *12*, 836–843.

[89] Abhervé, A.; Mañas-Valero, S.; Clemente-León, M.; Coronado, E. Graphene related magnetic materials: Micromechanical exfoliation of 2D layered magnets based on bimetallic anilate complexes with inserted $[Fe^{III}(acac_2\text{-trien})]^+$ and $[Fe^{III}(sal_2\text{-trien})]^+$ molecules. *Chem. Sci.* **2015**, *6*, 4665–4673.

[90] Deng, T.; Lu, Y.; Zhang, W.; Sui, M.; Shi, X. Y.; Wang, D.; Zheng, W. T. Inverted design for high-performance supercapacitor via $Co(OH)_2$-derived highly oriented MOF electrodes. *Adv. Energy Mater.* **2018**, *8*, 1702294.

[91] Ge, K.; Sun, S. J.; Zhao, Y.; Yang, K.; Wang, S.; Zhang, Z. H.; Cao, J. Y.; Yang, Y. F.; Zhang, Y.; Pan, M. W. et al. Facile synthesis of two-dimensional iron/cobalt metal-organic framework for efficient oxygen evolution electrocatalysis. *Angew. Chem., Int. Ed.* **2021**, *60*, 12097–12102.

[92] Song, D. Q.; Guo, H. Z.; Huang, K.; Zhang, H. Y.; Chen, J.; Wang, L.; Lian, C.; Wang, Y. Carboxylated carbon quantum dot-induced binary metal-organic framework nanosheet synthesis to boost the electrocatalytic performance. *Mater. Today* **2022**, *54*, 42–51.

[93] Jiang, M.; Li, J.; Cai, X. F.; Zhao, Y.; Pan, L. J.; Cao, Q. Q.; Wang, D. H.; Du, Y. W. Ultrafine bimetallic phosphide nanoparticles embedded in carbon nanosheets: Two-dimensional metal-organic framework-derived non-noble electrocatalysts for the highly efficient oxygen evolution reaction. *Nanoscale* **2018**, *10*, 19774–19780.

[94] Hu, X. Y.; Tan, P. F.; Dong, R.; Jiang, M.; Lu, L. L.; Wang, Y.; Liu, H. Q.; Liu, Y.; Xie, J. P.; Pan, J. A novel metal-organic framework intermediated synthesis of heterogeneous CoS_2/CoS porous nanosheets for enhanced oxygen evolution reaction. *Energy Technol.* **2021**, *9*, 2000961.

[95] Hu, Q.; Huang, X. W.; Wang, Z. Y.; Li, G. M.; Han, Z.; Yang, H. P.; Ren, X. Z.; Zhang, Q. L.; Liu, J. H.; He, C. X. Unconventionally fabricating defect-rich NiO nanoparticles within ultrathin metal-organic framework nanosheets to enable high-output oxygen evolution. *J. Mater. Chem. A* **2020**, *8*, 2140–2146.

[96] Li, H.; Ke, F.; Zhu, J. F. MOF-derived ultrathin cobalt phosphide nanosheets as efficient bifunctional hydrogen evolution reaction and oxygen evolution reaction electrocatalysts. *Nanomaterials* **2018**, *8*, 89.

[97] Lin, Y. F.; Wan, H.; Wu, D.; Chen, G.; Zhang, N.; Liu, X. H.; Li, J. H.; Cao, Y. J.; Qiu, G. Z.; Ma, R. Z. Metal-organic framework hexagonal nanoplates: Bottom-up synthesis, topotactic transformation, and efficient oxygen evolution reaction. *J. Am. Chem. Soc.* **2020**, *142*, 7317–7321.

[98] Srinivas, K.; Lu, Y. J.; Chen, Y. F.; Zhang, W. L.; Yang, D. X. $FeNi_3$-Fe_3O_4 heterogeneous nanoparticles anchored on 2D MOF nanosheets/1D CNT matrix as highly efficient bifunctional electrocatalysts for water splitting. *ACS Sustainable Chem. Eng.* **2020**, *8*, 3820–3831.

[99] Yuan, M. L.; Dipazir, S.; Wang, M.; Sun, Y.; Gao, D. L.; Bai, Y. L.; Zhang, M.; Lu, P. L.; He, H. Y.; Zhu, X. Y. et al. Polyoxometalate-assisted formation of CoSe/$MoSe_2$ heterostructures with enhanced oxygen evolution activity. *J. Mater. Chem. A* **2019**, *7*, 3317–3326.

[100] Huang, L.; Gao, G.; Zhang, H.; Chen, J. X.; Fang, Y. X.; Dong, S. J. Self-dissociation-assembly of ultrathin metal-organic framework nanosheet arrays for efficient oxygen evolution. *Nano Energy* **2020**, *68*, 104296.

[101] Jayaramulu, K.; Dubal, D. P.; Schneemann, A.; Ranc, V.; Perez-Reyes, C.; Stráská, J.; Kment, Š.; Otyepka, M.; Fischer, R. A.; Zbořil, R. Shape-assisted 2D MOF/graphene derived hybrids as exceptional lithium-ion battery electrodes. *Adv. Funct. Mater.* **2019**, *29*, 1902539.

[102] Meng, J. J.; Zhou, Y.; Chi, H. H.; Li, K.; Wan, J. M.; Hu, Z. W. Bimetallic porphyrin MOF anchored onto rGO nanosheets as a highly efficient 2D electrocatalyst for oxygen evolution reaction in alkaline conditions. *ChemistrySelect* **2019**, *4*, 8661–8670.

[103] Yang, C.; Cai, W. J.; Yu, B. B.; Qiu, H.; Li, M. L.; Zhu, L. W.; Yan, Z.; Hou, L.; Wang, Y. Y. Performance enhancement of oxygen evolution reaction through incorporating bimetallic electrocatalysts in two-dimensional metal-organic frameworks. *Catal. Sci. Technol.* **2020**, *10*, 3897–3903.

[104] Li, Y.; Gao, Z. G.; Bao, H. M.; Zhang, B. H.; Wu, C.; Huang, C. F.; Zhang, Z. L.; Xie, Y. Y.; Wang, H. Amorphous nickel-cobalt bimetal-organic framework nanosheets with crystalline motifs enable efficient oxygen evolution reaction: Ligands hybridization engineering. *J. Energy Chem.* **2021**, *53*, 251–259.

[105] Lu, M. T.; Li, Y. W.; He, P. P.; Cong, J. K.; Chen, D. N.; Wang, J. W.; Wu, Y. H.; Xu, H.; Gao, J. K.; Yao, J. M. Bimetallic metal-organic framework nanosheets as efficient electrocatalysts for oxygen evolution reaction. *J. Solid State Chem.* **2019**, *272*, 32–37.

[106] Zhuang, L. Z.; Ge, L.; Liu, H. L.; Jiang, Z. R.; Jia, Y.; Li, Z. H.; Yang, D. J.; Hocking, R. K.; Li, M. R.; Zhang, L. Z. et al. A surfactant-free and scalable general strategy for synthesizing ultrathin two-dimensional metal-organic framework nanosheets for the oxygen evolution reaction. *Angew. Chem., Int. Ed.* **2019**, *58*, 13565–13572.

[107] Han, M. Y.; Zhang, X. W.; Gao, H. Y.; Chen, S. Y.; Cheng, P.; Wang, P.; Zhao, Z. Y.; Dang, R.; Wang, G. *In situ* semi-sacrificial template-assisted growth of ultrathin metal-organic framework nanosheets for electrocatalytic oxygen evolution. *Chem. Eng. J.* **2021**, *426*, 131348.

[108] Li, W. X.; Fang, W.; Wu, C.; Dinh, K. N.; Ren, H.; Zhao, L.; Liu, C. T.; Yan, Q. Y. Bimetal-MOF nanosheets as efficient bifunctional electrocatalysts for oxygen evolution and nitrogen reduction reaction. *J. Mater. Chem. A* **2020**, *8*, 3658–3666.

[109] Xu, J.; Zhu, X.; Jia, X. L. From low- to high-crystallinity bimetal-organic framework nanosheet with highly exposed boundaries: An efficient and stable electrocatalyst for oxygen evolution reaction. *ACS Sustainable Chem. Eng.* **2019**, *7*, 16629–16639.

[110] Wang, C. P.; Liu, H. Y.; Bian, G.; Gao, X. X.; Zhao, S. C.; Kang,

Y.; Zhu, J.; Bu, X. H. Metal-layer assisted growth of ultralong quasi-2D MOF nanoarrays on arbitrary substrates for accelerated oxygen evolution. *Small* **2019**, *15*, 1906086.
[111] Thangasamy, P.; Shanmuganathan, S.; Subramanian, V. A NiCo-MOF nanosheet array based electrocatalyst for the oxygen evolution reaction. *Nanoscale Adv.* **2020**, *2*, 2073–2079.
[112] Jia, J. W.; Wei, L. F.; Li, F.; Yu, C. L.; Yang, K.; Liang, T. X. *In situ* growth of NiFe MOF/NF by controlling solvent mixtures as efficient electrocatalyst in oxygen evolution. *Inorg. Chem. Commun.* **2021**, *128*, 108605.
[113] Rui, K.; Zhao, G. Q.; Chen, Y. P.; Lin, Y.; Zhou, Q.; Chen, J. Y.; Zhu, J. X.; Sun, W. P.; Huang, W.; Dou, S. X. Hybrid 2D dual-metal-organic frameworks for enhanced water oxidation catalysis. *Adv. Funct. Mater.* **2018**, *28*, 1801554.
[114] Liu, M. J.; Zheng, W. R.; Ran, S. J.; Boles, S. T.; Lee, L. Y. S. Overall water-splitting electrocatalysts based on 2D CoNi-metal-organic frameworks and its derivative. *Adv. Mater. Interfaces* **2018**, *5*, 1800849.
[115] Pan, C. C.; Liu, Z. C.; Huang, M. H. 2D iron-doped nickel MOF nanosheets grown on nickel foam for highly efficient oxygen evolution reaction. *Appl. Surf. Sci.* **2020**, *529*, 147201.
[116] Bai, Y.; Zhang, G. X.; Zheng, S. S.; Li, Q.; Pang, H.; Xu, Q. Pyridine-modulated Ni/Co bimetallic metal-organic framework nanoplates for electrocatalytic oxygen evolution. *Sci. China Mater.* **2021**, *64*, 137–148.
[117] Xing, D. N.; Wang, Y. Y.; Zhou, P.; Liu, Y. Y.; Wang, Z. Y.; Wang, P.; Zheng, Z. K.; Cheng, H. F.; Dai, Y.; Huang, B. B. Co_3(hexaiminotriphenylene)$_2$: A conductive two-dimensional π-d conjugated metal-organic framework for highly efficient oxygen evolution reaction. *Appl. Catal. B: Environ.* **2020**, *278*, 119295.
[118] Mu, X. Q.; Yuan, H. M.; Jing, H. Y.; Xia, F. J.; Wu, J. S.; Gu, X. Y.; Chen, C. Y.; Bao, J. C.; Liu, S. L.; Mu, S. C. Superior electrochemical water oxidation in vacancy defect-rich 1.5 nm ultrathin trimetal-organic framework nanosheets. *Appl. Catal. B: Environ.* **2021**, *296*, 120095.
[119] Shrestha, N. K.; Patil, S. A.; Cho, S.; Jo, Y.; Kim, H.; Im, H. Cu-Fe-NH_2 based metal-organic framework nanosheets via drop-casting for highly efficient oxygen evolution catalysts durable at ultrahigh currents. *J. Mater. Chem. A* **2020**, *8*, 24408–24418.
[120] Wang, J. L.; Zhang, M. L.; Li, J. H.; Jiao, F. X.; Lin, Y.; Gong, Y. Q. A highly efficient electrochemical oxygen evolution reaction catalyst constructed from a S-treated two-dimensional Prussian blue analogue. *Dalton Trans.* **2020**, *49*, 14290–14296.
[121] Jia, Y. T.; Xu, Z. K.; Li, L.; Lin, S. Y. Formation of NiFe-MOF nanosheets on Fe foam to achieve advanced electrocatalytic oxygen evolution. *Dalton Trans.* **2022**, *51*, 5053–5060.
[122] Li, F. L.; Wang, P. T.; Huang, X. Q.; Young, D. J.; Wang, H. F.; Braunstein, P.; Lang, J. P. Large-scale, bottom-up synthesis of binary metal-organic framework nanosheets for efficient water oxidation. *Angew. Chem., Int. Ed.* **2019**, *58*, 7051–7056.
[123] Chen, X. D.; Chen, Y.; Shen, Z. F.; Song, C. Y.; Ji, P. Y.; Wang, N. N.; Su, D. W.; Wang, Y. G.; Wang, G. X.; Cui, L. F. Self-crosslinkable polyaniline with coordinated stabilized CoOOH nanosheets as a high-efficiency electrocatalyst for oxygen evolution reaction. *Appl. Surf. Sci.* **2020**, *529*, 147173.
[124] Jiang, W.; Ni, X. J.; Liu, F. Exotic topological bands and quantum states in metal-organic and covalent-organic frameworks. *Acc. Chem. Res.* **2021**, *54*, 416–426.
[125] Yang, D. R.; Wang, X. 2D π-conjugated metal-organic frameworks for CO_2 electroreduction. *SmartMat.* **2022**, *3*, 54–67.
[126] Liu, X. H.; Yang, Y. W.; Liu, X. M.; Hao, Q.; Wang, L. M.; Sun, B.; Wu, J.; Wang, D. Confined synthesis of oriented two-dimensional Ni_3(hexaiminotriphenylene)$_2$ films for electrocatalytic oxygen evolution reaction. *Langmuir* **2020**, *36*, 7528–7532.
[127] Wang, J. R.; Fan, Y. C.; Qi, S. Y.; Li, W. F.; Zhao, M. W. Bifunctional HER/OER or OER/ORR catalytic activity of two-dimensional TM_3(HITP)$_2$ with TM = Fe-Zn. *J. Phys. Chem. C* **2020**, *124*, 9350–9359.
[128] Li, C.; Shi, L. L.; Zhang, L. L.; Chen, P.; Zhu, J. W.; Wang, X.; Fu, Y. S. Ultrathin two-dimensional π-d conjugated coordination polymer Co_3(Hexaaminobenzene)$_2$ nanosheets for highly efficient oxygen evolution. *J. Mater. Chem. A* **2020**, *8*, 369–379.
[129] Li, C.; Gao, Y. T.; Xia, X. F.; Zhu, J. W.; Wang, X.; Fu, Y. S. Hierarchically structured two-dimensional bimetallic CoNi-hexaaminobenzene coordination polymers derived from $Co(OH)_2$ for enhanced oxygen evolution catalysis. *Small* **2020**, *16*, 1907043.
[130] Yang, S. X.; Yu, Y. H.; Gao, X. J.; Zhang, Z. P.; Wang, F. Recent advances in electrocatalysis with phthalocyanines. *Chem. Soc. Rev.* **2021**, *50*, 12985–13011.
[131] Jia, H. X.; Yao, Y. C.; Zhao, J. T.; Gao, Y. Y.; Luo, Z. L.; Du, P. W. A novel two-dimensional nickel phthalocyanine-based metal-organic framework for highly efficient water oxidation catalysis. *J. Mater. Chem. A* **2018**, *6*, 1188–1195.
[132] Jayaramulu, K.; Masa, J.; Morales, D. M.; Tomanec, O.; Ranc, V.; Petr, M.; Wilde, P.; Chen, Y. T.; Zboril, R.; Schuhmann, W. et al. Ultrathin 2D cobalt zeolite-imidazole framework nanosheets for electrocatalytic oxygen evolution. *Adv. Sci.* **2018**, *5*, 1801029.
[133] Xiao, Z. J.; Xu, F. A two-dimensional zeolitic imidazolate framework loaded with an acrylate-substituted oxoiron cluster as an efficient electrocatalyst for the oxygen evolution reaction. *New J. Chem.* **2022**, *46*, 11095–11100.
[134] Li, D. J.; Li, Q. H.; Gu, Z. G.; Zhang, J. A surface-mounted MOF thin film with oriented nanosheet arrays for enhancing the oxygen evolution reaction. *J. Mater. Chem. A* **2019**, *7*, 18519–18528.
[135] Guo, C. X.; Jiao, Y.; Zheng, Y.; Luo, J.; Davey, K.; Qiao, S. Z. Intermediate modulation on noble metal hybridized to 2D metal-organic framework for accelerated water electrocatalysis. *Chem* **2019**, *5*, 2429–2441.
[136] Chi, Y.; Yang, W. P.; Xing, Y. C.; Li, Y.; Pang, H.; Xu, Q. Ni/Co bimetallic organic framework nanosheet assemblies for high-performance electrochemical energy storage. *Nanoscale* **2020**, *12*, 10685–10692.
[137] Zeng, X. J.; Shui, J. L.; Liu, X. F.; Liu, Q. T.; Li, Y. C.; Shang, J. X.; Zheng, L. R.; Yu, R. H. Single-atom to single-atom grafting of Pt_1 onto Fe-N_4 center: Pt_1@Fe-N-C multifunctional electrocatalyst with significantly enhanced properties. *Adv. Energy Mater.* **2018**, *8*, 1701345.
[138] Zou, Z. H.; Wang, J. L.; Pan, H. R.; Li, J.; Guo, K. L.; Zhao, Y. Q.; Xu, C. L. Enhanced oxygen evolution reaction of defective CoP/MOF-integrated electrocatalyst by partial phosphating. *J. Mater. Chem. A* **2020**, *8*, 14099–14105.
[139] Cong, J. K.; Xu, H.; Lu, M. T.; Wu, Y. H.; Li, Y. W.; He, P. P.; Gao, J. K.; Yao, J. M.; Xu, S. Q. Two-dimensional Co@N-carbon nanocomposites facilely derived from metal-organic framework nanosheets for efficient bifunctional electrocatalysis. *Chem. Asian J.* **2018**, *13*, 1485–1491.
[140] Wei, X. D.; Li, N.; Liu, N. Ultrathin NiFeZn-MOF nanosheets containing few metal oxide nanoparticles grown on nickel foam for efficient oxygen evolution reaction of electrocatalytic water splitting. *Electrochim. Acta* **2019**, *318*, 957–965.
[141] He, K.; Cao, Z.; Liu, R. R.; Miao, Y.; Ma, H. Y.; Ding, Y. *In situ* decomposition of metal-organic frameworks into ultrathin nanosheets for the oxygen evolution reaction. *Nano Res.* **2016**, *9*, 1856–1865.
[142] Liu, J. L.; Gao, Y.; Tang, X. X.; Zhan, K.; Zhao, B.; Xia, B. Y.; Yan, Y. Metal-organic framework-derived hierarchical ultrathin CoP nanosheets for overall water splitting. *J. Mater. Chem. A* **2020**, *8*, 19254–19261.
[143] Xia, Q. H.; Liu, H. M.; Jin, M. M.; Lai, L. F.; Qiu, Y. T.; Zhai, H. L.; Li, H. B.; Liu, X. Catalysts confined inside CNTS derived from 2D metal-organic frameworks for electrolysis. *Nanoscale* **2020**, *12*, 8969–8974.
[144] Tian, J. Y.; Jiang, F. L.; Yuan, D. Q.; Zhang, L. J.; Chen, Q. H.; Hong, M. C. Electric-field assisted *in situ* hydrolysis of bulk metal-organic frameworks (MOFs) into ultrathin metal oxyhydroxide nanosheets for efficient oxygen evolution. *Angew. Chem., Int. Ed.* **2020**, *59*, 13101–13108.
[145] Chen, W. B.; Wang, C. S.; Su, S. B.; Wang, H.; Cai, D. D. Synthesis of ZIF-9(III)/Co LDH layered composite from ZIF-9(I) based on controllable phase transition for enhanced electrocatalytic

oxygen evolution reaction. *Chem. Eng. J* **2021**, *414*, 128784.
[146] Li, Y. L.; Jia, B. M.; Chen, B. Y.; Liu, Q. L.; Cai, M. K.; Xue, Z. Q.; Fan, Y. N.; Wang, H. P.; Su, C. Y.; Li, G. Q. MOF-derived Mn doped porous CoP nanosheets as efficient and stable bifunctional electrocatalysts for water splitting. *Dalton Trans.* **2018**, *47*, 14679–14685.
[147] Lin, Y. F.; Chen, G.; Wan, H.; Chen, F. S.; Liu, X. H.; Ma, R. Z. 2D free-standing nitrogen-doped Ni-Ni_3S_2@carbon nanoplates derived from metal-organic frameworks for enhanced oxygen evolution reaction. *Small* **2019**, *15*, 1900348.
[148] Xu, Y.; Tu, W. G.; Zhang, B. W.; Yin, S. M.; Huang, Y. Z.; Kraft, M.; Xu, R. Nickel nanoparticles encapsulated in few-layer nitrogen-doped graphene derived from metal-organic frameworks as efficient bifunctional electrocatalysts for overall water splitting. *Adv. Mater.* **2017**, *29*, 1605957.
[149] Wang, C.; Shang, H. Y.; Wang, Y.; Li, J.; Guo, S. Y.; Guo, J.; Du, Y. K. A general MOF-intermediated synthesis of hollow CoFe-based trimetallic phosphides composed of ultrathin nanosheets for boosting water oxidation electrocatalysis. *Nanoscale* **2021**, *13*, 7279–7284.
[150] Chen, W. X.; Zhang, Y. W.; Chen, G. L.; Huang, R.; Wu, Y. J.; Zhou, Y. M.; Hu, Y. J.; Ostrikov, K. Hierarchical porous bimetal-sulfide bi-functional nanocatalysts for hydrogen production by overall water electrolysis. *J. Colloid Interface Sci.* **2020**, *560*, 426–435.
[151] Jiang, Q. Y.; Xu, J.; Li, Z. Q.; Zhou, C. H.; Chen, X.; Meng, H. B.; Han, Y.; Shi, X. F.; Zhan, C. H.; Zhang, Y. Q. et al. Two-dimensional metal-organic framework nanosheet supported noble metal nanocrystals for high-efficiency water oxidation. *Adv. Mater. Interfaces* **2021**, *8*, 2002034.
[152] Yu, R.; Liu, D. M.; Yuan, M. Y.; Wang, Y.; Ye, C. Q.; Li, J.; Du, Y. K. Universal MOF-mediated synthesis of 2D CoNi-based layered triple hydroxides electrocatalyst for efficient oxygen evolution reaction. *J. Colloid Interface Sci.* **2021**, *602*, 612–618.
[153] Lu, Z. J.; Wang, K.; Cao, Y. L.; Li, Y. Z.; Jia, D. Z. Amino-functionalized iron-based MOFs modified with 2D $FeCo(OH)_x$ hybrids for boosting oxygen evolution. *J. Alloys Compd.* **2021**, *871*, 159580.
[154] Zhang, W. D.; Yu, H.; Li, T.; Hu, Q. T.; Gong, Y.; Zhang, D. Y.; Liu, Y.; Fu, Q. T.; Zhu, H. Y.; Yan, X. D. et al. Hierarchical trimetallic layered double hydroxide nanosheets derived from 2D metal-organic frameworks for enhanced oxygen evolution reaction. *Appl. Catal. B: Environ.* **2020**, *264*, 118532.
[155] Wang, Y. R.; Wang, A.; Xue, Z. Z.; Wang, L.; Li, X. Y.; Wang, G. M. Ultrathin metal-organic framework nanosheet arrays and derived self-supported electrodes for overall water splitting. *J. Mater. Chem. A* **2021**, *9*, 22597–22602.
[156] Wang, X. L.; Xiao, H.; Li, A.; Li, Z.; Liu, S. J.; Zhang, Q. H.; Gong, Y.; Zheng, L. R.; Zhu, Y. Q.; Chen, C. et al. Constructing NiCo/Fe_3O_4 heteroparticles within MOF-74 for efficient oxygen evolution reactions. *J. Am. Chem. Soc.* **2018**, *140*, 15336–15341.
[157] Liu, H. B.; Huang, R.; Chen, W. X.; Zhang, Y. W.; Wang, M. M.; Hu, Y. J.; Zhou, Y. M.; Song, Y. C. Porous 2D cobalt-nickel phosphide triangular nanowall architecture assembled by 3D microsphere for enhanced overall water splitting. *Appl. Surf. Sci.* **2021**, *569*, 150762.
[158] Zhao, M.; Li, W.; Li, J. Y.; Hu, W. H.; Li, C. M. Strong electronic interaction enhanced electrocatalysis of metal sulfide clusters embedded metal-organic framework ultrathin nanosheets toward highly efficient overall water splitting. *Adv. Sci.* **2020**, *7*, 2001965.
[159] Chen, B.; Kim, D.; Zhang, Z.; Lee, M.; Yong, K. MOF-derived NiCoZnP nanoclusters anchored on hierarchical N-doped carbon nanosheets array as bifunctional electrocatalysts for overall water splitting. *Chem. Eng. J.* **2021**, *422*, 130533.
[160] Xu, S. X.; Du, J.; Li, J. Y.; Sun, L. C.; Li, F. Nickel-selenide templated binary metal-organic frameworks for efficient water oxidation. *J. Mater. Chem. A* **2020**, *8*, 16908–16912.
[161] Bian, J. L.; Song, Z. Y.; Li, X. L.; Zhang, Y. Z.; Cheng, C. W. Nickel iron phosphide ultrathin nanosheets anchored on nitrogen-doped carbon nanoflake arrays as a bifunctional catalyst for efficient overall water splitting. *Nanoscale* **2020**, *12*, 8443–8452.
[162] Zhao, S. L.; Tan, C. H.; He, C. T.; An, P. F.; Xie, F.; Jiang, S.; Zhu, Y. F.; Wu, K. H.; Zhang, B. W.; Li, H. J. et al. Structural transformation of highly active metal-organic framework electrocatalysts during the oxygen evolution reaction. *Nat. Energy* **2020**, *5*, 881–890.
[163] Zheng, W. R.; Lee, L. Y. S. Metal-organic frameworks for electrocatalysis: Catalyst or precatalyst. *ACS Energy Lett.* **2021**, *6*, 2838–2843.
[164] Yuan, S.; Peng, J. Y.; Cai, B.; Huang, Z. H.; Garcia-Esparza, A. T.; Sokaras, D.; Zhang, Y. R.; Giordano, L.; Akkiraju, K.; Zhu, Y. G. et al. Tunable metal hydroxide-organic frameworks for catalysing oxygen evolution. *Nat. Mater.* **2022**, *21*, 673–680.
[165] Zhu, D. D.; Liu, J. L.; Wang, L.; Du, Y.; Zheng, Y.; Davey, K.; Qiao, S. Z. A 2D metal-organic framework/$Ni(OH)_2$ heterostructure for an enhanced oxygen evolution reaction. *Nanoscale* **2019**, *11*, 3599–3605.
[166] Zheng, F. Q.; Zhang, W. F.; Zhang, X. X.; Zhang, Y. L.; Chen, W. Sub-2 nm ultrathin and robust 2D FeNi layered double hydroxide nanosheets packed with 1D FeNi-MOFs for enhanced oxygen evolution electrocatalysis. *Adv. Funct. Mater.* **2021**, *31*, 2103318.
[167] Han, C.; Zhong, L.; Sun, Q. H.; Chen, D. D.; Li, T. T.; Hu, Y.; Qian, J. J.; Huang, S. M. Electrochemical evolution of cobalt-carboxylate framework for efficient water oxidation. *J. Power Sources* **2021**, *499*, 229947.
[168] Cui, C.; Wang, J. Y.; Luo, Z. G.; Wang, J.; Li, C. X.; Li, Z. Q. MOF-mediated synthesis of monodisperse $Co(OH)_2$ flower-like nanosheets for enhanced oxygen evolution reaction. *Electrochim. Acta* **2018**, *273*, 327–334.
[169] Chen, D.; Yu, J. H.; Cui, Z. X.; Zhang, Q.; Chen, X.; Sui, J.; Dong, H. Z.; Yu, L. Y.; Dong, L. F. Hierarchical architecture derived from two-dimensional zeolitic imidazolate frameworks as an efficient metal-based bifunctional oxygen electrocatalyst for rechargeable Zn-air batteries. *Electrochim. Acta* **2020**, *331*, 135394.
[170] Chen, W. X.; Zhang, Y. W.; Chen, G. L.; Huang, R.; Zhou, Y. M.; Wu, Y. J.; Hu, Y. J.; Ostrikov, K. Mesoporous cobalt-iron-organic frameworks: A plasma-enhanced oxygen evolution electrocatalyst. *J. Mater. Chem. A* **2019**, *7*, 3090–3100.
[171] Rodenas, T.; Beeg, S.; Spanos, I.; Neugebauer, S.; Girgsdies, F.; Algara-Siller, G.; Schleker, P. P. M.; Jakes, P.; Pfänder, N.; Willinger, M. et al. 2D metal organic framework-graphitic carbon nanocomposites as precursors for high-performance O_2-evolution electrocatalysts. *Adv. Energy Mater.* **2018**, *8*, 1802404.
[172] Wei, G. J.; Zhou, Z.; Zhao, X. X.; Zhang, W. Q.; An, C. H. Ultrathin metal-organic framework nanosheet-derived ultrathin Co_3O_4 nanomeshes with robust oxygen-evolving performance and asymmetric supercapacitors. *ACS Appl. Mater. Interfaces* **2018**, *10*, 23721–23730.
[173] He, P. C.; Xie, Y. B.; Dou, Y. B.; Zhou, J.; Zhou, A. W.; Wei, X.; Li, J. R. Partial sulfurization of a 2D MOF array for highly efficient oxygen evolution reaction. *ACS Appl. Mater. Interfaces* **2019**, *11*, 41595–41601.
[174] Zhao, J. Y.; Wang, R.; Wang, S.; Lv, Y. R.; Xu, H.; Zang, S. Q. Metal-organic framework-derived Co_9S_8 embedded in N, O and S-tridoped carbon nanomaterials as an efficient oxygen bifunctional electrocatalyst. *J. Mater. Chem. A* **2019**, *7*, 7389–7395.
[175] Zhai, M. K.; Wang, F.; Du, H. B. Transition-metal phosphide-carbon nanosheet composites derived from two-dimensional metal-organic frameworks for highly efficient electrocatalytic water-splitting. *ACS Appl. Mater. Interfaces* **2017**, *9*, 40171–40179.
[176] Wang, H. W.; Li, Y. J.; Wang, R.; He, B. B.; Gong, Y. S. Metal-organic-framework template-derived hierarchical porous CoP arrays for energy-saving overall water splitting. *Electrochim. Acta* **2018**, *284*, 504–512.
[177] Xia, Z. X.; Fang, J.; Zhang, X. M.; Fan, L. P.; Barlow, A. J.; Lin, T.; Wang, S. L.; Wallace, G. G.; Sun, G. Q.; Wang, X. G. Pt nanoparticles embedded metal-organic framework nanosheets: A synergistic strategy towards bifunctional oxygen electrocatalysis. *Appl. Catal. B: Environ.* **2019**, *245*, 389–398.
[178] Low, J. J.; Benin, A. I.; Jakubczak, P.; Abrahamian, J. F.; Faheem, S. A.; Willis, R. R. Virtual high throughput screening confirmed experimentally: Porous coordination polymer hydration. *J. Am.*

Chem. Soc. **2009**, *131*, 15834–15842.

[179] Hu, Q.; Qin, Y. J.; Wang, X. D.; Zheng, H. J.; Gao, K. R.; Yang, H. P.; Zhang, P. X.; Shao, M. H.; He, C. X. Grain boundaries engineering of hollow copper nanoparticles enables highly efficient ammonia electrosynthesis from nitrate. *CCS Chem.* **2022**, *4*, 2053–2064.

[180] Dai, F. N.; Wang, X. K.; Zheng, S. H.; Sun, J. P.; Huang, Z. D.; Xu, B.; Fan, L. L.; Wang, R. M.; Sun, D. F.; Wu, Z. S. Toward high-performance and flexible all-solid-state micro-supercapacitors: MOF bulk vs. MOF nanosheets. *Chem. Eng. J.* **2021**, *413*, 127520.

[181] Wang, L. J.; Saji, S. E.; Wu, L. J.; Wang, Z. X.; Chen, Z. J.; Du, Y. P.; Yu, X. F.; Zhao, H. T.; Yin, Z. Y. Emerging synthesis strategies of 2D MOFs for electrical devices and integrated circuits. *Small* **2022**, *18*, 2201642.

[182] Rodenas, T.; Luz, I.; Prieto, G.; Seoane, B.; Miro, H.; Corma, A.; Kapteijn, F.; Llabrés i Xamena, F. X.; Gascon, J. Metal-organic framework nanosheets in polymer composite materials for gas separation. *Nat. Mater.* **2015**, *14*, 48–55.

[183] Cao, L. Y.; Lin, Z. K.; Peng, F.; Wang, W. W.; Huang, R. Y.; Wang, C.; Yan, J. W.; Liang, J.; Zhang, Z. M.; Zhang, T. et al. Self-supporting metal-organic layers as single-site solid catalysts. *Angew. Chem., Int. Ed.* **2016**, *55*, 4962–4966.

[184] Gao, G. P.; Waclawik, E. R.; Du, A. J. Computational screening of two-dimensional coordination polymers as efficient catalysts for oxygen evolution and reduction reaction. *J. Catal.* **2017**, *352*, 579–585.